A Volcano Rekindled: The Renewed Eruption of Mount St. Helens, 2004–2006
Edited by David R. Sherrod, William E. Scott, and Peter H. Stauffer
U.S. Geological Survey Professional Paper 1750, 2008

Chapter 15

Analysis of GPS-Measured Deformation Associated with the 2004–2006 Dome-Building Eruption of Mount St. Helens, Washington

By Michael Lisowski[1], Daniel Dzurisin[1], Roger P. Denlinger[1], and Eugene Y. Iwatsubo[1]

Abstract

Detecting far-field deformation at Mount St. Helens since the crater-forming landslide and blast in 1980 has been difficult despite frequent volcanic activity and improved monitoring techniques. Between 1982 and 1991, the systematic extension of line lengths in a regional GPS trilateration network is consistent with recharge of a deep magma chamber during that interval. The rate of extension, however, averages only 3 mm/yr, and some of this apparent deformation may result from systematic scale error in the electronic distance measurements. Subsequent GPS surveys and data from a continuous GPS station, located 9 km north of Mount St. Helens and operating since 1997, show no significant volcanic deformation until the start of unrest on September 23, 2004. The current eruption has been accompanied by subtle but widespread inward and downward movement of GPS monitoring stations, exponentially decreasing with time and totaling as much as 30 mm. The observed deformation is consistent with the predictions of an elastic half-space model of a vertically elongate magma chamber with its center at a depth of around 7 to 8 km and with a total cavity-volume loss of about $16–24\times10^6$ m^3. The discrepancy between the estimated cavity-volume loss and the $>83\times10^6$-m^3 volume of the erupted dome can be explained, for the most part, by exsolution of gas in the stored magma and by minor input of new magma during the eruption.

Introduction

The current episode of volcanic unrest at Mount St. Helens began suddenly with a shallow earthquake swarm on September 23, 2004. Geodetic monitoring of deformation in the months before and days after the start of unrest was limited to data from a single, continuous, dual-frequency GPS (CGPS) station, JRO1 (installed in 1997), having an antenna on the roof of Johnston Ridge Observatory (JRO) (fig. 1). Regional deformation in the years before the start of unrest was measured using campaign-style GPS surveys of a 43-station network during the summers of 2000 and 2003. Annual surveys of background deformation in the crater of Mount St. Helens began in 2000 at six GPS stations on and near the 1980s dome ("old dome") for the purpose of ground control (Schilling and others, this volume, chap. 8). A network of three single-frequency (L1) CGPS stations was installed in 2000 to monitor deformation on the September 1984 lobe of the 1980s dome, relative to two stations just outside of the crater (LaHusen and others, this volume, chap. 16). Only one of these L1 CGPS stations, SFOT (on the west flank), remained operational during most of 2004, and there is no GPS measurement of deformation in the crater until September 28, 2004. In the 1980s and 1990s, deformation of Mount St. Helens was measured by using (1) electronic distance meters (EDM) to track line-length changes, (2) theodolites to track angle changes, and (3) level arrays and electronic tiltmeters to monitor ground tilt (Dvorak and others, 1981; Lipman and others, 1981; Swanson and others, 1981; Ewert and Swanson, 1992).

The observed patterns and rates of deformation in volcanic areas are used to constrain possible sources and mechanisms of volcanic unrest. We did not detect a systematic pattern of deformation, other than secular tectonic motion, between the 2000 and 2003 campaign GPS surveys; nor were there anomalies in the JRO1 CGPS three-dimensional (3D), position-component time series before the start of unrest. By the time of the first phreatic explosion on October 1, 2004, the L1 CGPS network was restored to operational condition (the station on the September 1984

[1]U.S. Geological Survey, 1300 SE Cardinal Court, Vancouver, WA 98683

lobe of the dome was destroyed by ballistics on October 1) and several campaign GPS stations on the volcano's flanks were occupied. Within two weeks, additional CGPS stations were installed by the Cascades Volcano Observatory (CVO) and the Plate Boundary Observatory (PBO). Displacement of these stations during the eruption was small (a few centimeters maximum) and consistently inward toward Mount St. Helens and downward, the pattern of movement expected if a deep magma chamber were being depleted during the eruption. The deformation, however, is small given the volume of lava erupted at the surface. The pressure loss in the deep magma chamber that is feeding the eruption may be compensated by recharge and by exsolution of gas (Mastin and others, this volume, chap. 22).

We begin by discussing our methods of GPS data reduction and analysis, emphasizing the technique used to improve measurement precision by removing common-mode noise. We then use regional GPS surveys and CGPS data to calculate the pattern and rate of background tectonic deformation and to derive a simple tectonic model. Local deformation near Mount St. Helens is then calculated from EDM-measured, line-length data collected during the 1980s and 1990s and from GPS-measured position-change data collected between 2000 and 2003; these results are compared with the predictions indicated in the tectonic model. The time series of deformation at CGPS station JRO1 is examined carefully for anomalies in the years before the start of the current episode of volcanic unrest at Mount St. Helens. Finally, eruption-related deformation is calculated, and an elastic, half-space model of a deflating, spheroidal magma chamber is used to fit the observed deformation.

Figure 1. Radome-covered antenna for CGPS station JRO1, on the roof of the U.S.D.A. Forest Service's Johnston Ridge Observatory, 9 km north of Mount St. Helens, Washington. In the weeks before and days after September 23, 2004, when seismic unrest began, JRO1 was the only GPS station operating within 40 km of the volcano. USGS photo by E.Y. Iwatsubo.

GPS Data Collection and Analysis

Campaign GPS and Continuous Dual-Frequency GPS Networks

Regional and local deformation around Mount St. Helens is measured episodically with campaign GPS surveys and continuously with CGPS stations (fig. 2). The following is a simplified discussion of how GPS positions are determined. The basic principal is that a GPS position can be triangulated from distance measurements to several known locations. The GPS satellites transmit encoded timing signals (pseudoranges) at two carrier frequencies, L1 (1575.42 MHz) and L2 (1227.60 MHz). The orbits of the satellites are predictable, making them reference points from which the ground position can be triangulated. The distance is measured directly by using the travel time of the coded signal, but it is called a pseudorange because the satellite and ground clocks used to measure the travel time of the one-way satellite transmission are not synchronized. The most accurate measurement of distance is obtained from the relatively short-wavelength, continuous L1 and L2 carrier signals and from the so-called "ionospheric free" linear combination of L1 and L2 known as LC or L3. Generally, the LC observable is used to minimize scale error introduced by fluctuations in ionospheric activity. With the carrier signals, the range to the satellite is expressed as the sum of the observed carrier phase plus an ambiguous integer number of carrier wavelengths. Methods have been developed to determine or "fix" the phase ambiguities to their correct integer values, which removes them as an unknown in the solution and improves measurement precision.

The GPS data discussed here are acquired with geodetic-quality receivers that record pseudorange and carrier-phase data at least every 60 s, and most often at rates of 30, 15, or 10 s. During campaign GPS surveys, we collect data for a minimum of 6 hours (usually 24 hours) on multiple days.

Most of the campaign GPS stations around Mount St. Helens were surveyed initially in 2000, with the last complete survey of the network in 2003. Several stations were surveyed after the start of unrest on September 23, 2004, and again in 2005 and 2006. The center-punched, permanent tablets marking the campaign GPS stations generally are set in bedrock to provide a stable, long-term, ground-reference point. The only measure of deformation near Mount St. Helens at the start of unrest was provided by CGPS station JRO1. Other CGPS stations, operated by the Pacific Northwest Geodetic Array (PANGA) and the National Geodetic Survey's Continuous Operating Reference Stations (CORS), are found in the surrounding region and serve as stable local reference stations. Following the initial seismic swarm, a small number of the campaign GPS stations were reoccupied to measure deformation accumulated since 2003 and possible ongoing deformation during the early stages of the eruption.

By mid-October 2004 a new network of CGPS stations, installed by the USGS–CVO and the National Science Foundation's PBO, were tracking deformation associated with the

eruption (table 1). Additional PBO and CVO CGPS stations were added in 2005 and 2006. In order to expedite obtaining site usage permits, and to keep the antennas above the winter snow pack, many of the new CGPS antennas were placed at the top of existing "winterized" 3- to 3.5-m-high steel towers that originally were installed in the fall of 1980 for EDM measurements (Swanson and others, 1981). Burial of the GPS antennas by snow has not been a problem, but ice buildup around the antenna and tower, particularly for stations high on the volcano's flank, has caused pseudodisplacements, two warped towers, and many communication and power failures.

GPS Data Processing: Minimally Constrained Daily Solution

We process GPS data with GIPSY/OASIS II software (Webb and Zumberge, 1995). Daily point-positioning solutions (Zumberge and others, 1997) use satellite orbit and clock

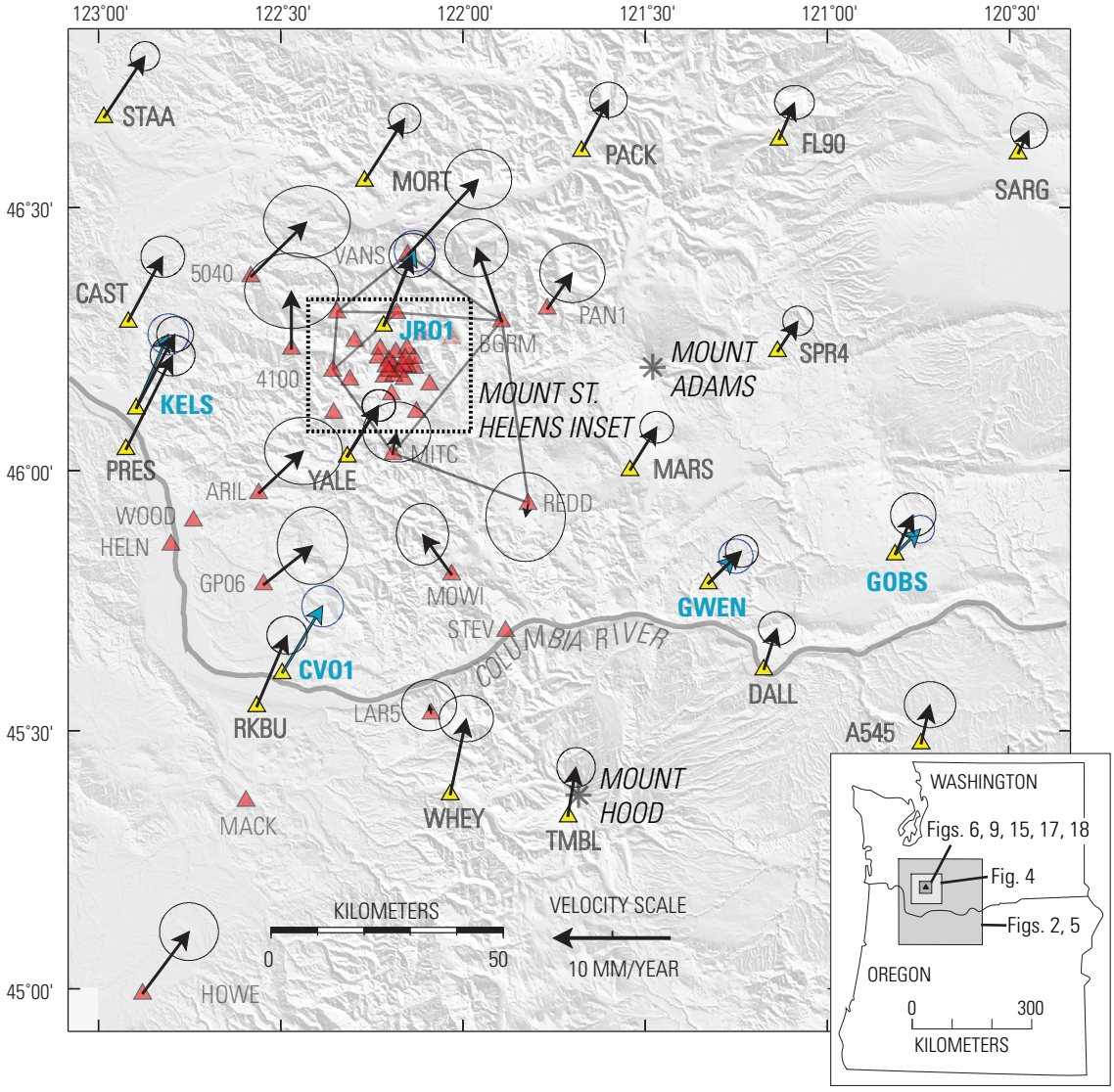

Figure 2. Map showing GPS stations in southwest Washington and northwest Oregon and their average horizontal-velocity vectors relative to stable North America (tipped with 95-percent-confidence error ellipses, vector scale at bottom) through September 2004. CGPS station names and velocity vectors are shown in blue. Black vectors at CGPS stations are calculated only from data coincident with campaign GPS surveys. Velocities at stations marked with yellow triangles are used to calculate background deformation for a tectonic model, which includes rigid-block motion and uniform-strain accumulation. The position of many stations was measured several times using campaign GPS, with some measurements made as early as 1992. However, the positions of most stations near Mount St. Helens (red triangles) were measured only in summers of 2000 and 2003. The Helens trilateration network, measured in 1982 and 1991, is shown here with faint solid lines between stations. The dashed box marks the local area around Mount St. Helens shown in figure 6.

Table 1. Regional and local continuously transmitting GPS (CGPS) stations near Mount St. Helens, Washington.

[Stations are listed in order of installation. PANGA, Pacific Northwest Geodetic Array; CVO, Cascades Volcano Observatory; PBO, Plate Boundary Observatory. See figure 2 for locations of most stations. Station names in bold type are within 20 km of Mount St. Helens.]

Station	Agency	Date operational	Monument type	Latitude (degrees)	Longitude (degrees)	Ellipsoidal elevation (m)
GOBS	PANGA	08/27/1997	Deep-drilled and braced	45.8388	-120.8147	621.49
KELS	PANGA	10/09/1997	Deep-drilled and braced	46.1182	-122.8961	-15.92
JRO1	CVO	05/23/1997	Roof mount	46.2751	-122.2176	1275.61
REDM	PANGA	07/24/1998	Shallow pier	44.2598	-121.1479	919.85
LIND	PANGA	07/28/1998	Roof mount	47.0003	-120.5390	471.93
LINH	PANGA	04/04/2002	Roof mount	47.0000	-120.5390	472.28
CVO1	CVO	01/04/2003	Roof mount	45.6109	-122.4961	66.67
P432	PBO	06/20/2004	Deep-drilled and braced	46.6228	-121.6832	318.88
P420	PBO	06/25/2004	Deep-drilled and braced	46.5886	-122.4961	74.11
P421	PBO	12/15/2004	Deep-drilled and braced	46.5318	-122.4292	220.60
TWRI	CVO	10/06/2004	EDM reflector tower	46.1979	-122.2119	2070.81
TWIW	CVO	10/11/2004	EDM reflector tower	46.2129	-122.1587	1630.55
P697	PBO	10/14/2004	EDM reflector tower	46.1876	-122.1766	2214.61
P693	PBO	10/14/2004	EDM reflector tower	46.2103	-122.2024	2113.00
P695	PBO	10/15/2004	EDM reflector tower	46.1990	-122.1642	2015.68
P696	PBO	10/15/2004	EDM reflector tower	46.1969	-122.1516	1600.03
TSTU	CVO	10/15/2004	EDM instrument tower	46.2369	-122.2241	1248.65
P687	PBO	10/16/2004	Shallow-drilled and braced	46.1096	-122.3546	391.10
TGAU	CVO	10/21/2004	EDM reflector tower	46.2192	-122.1923	1618.28
P698	PBO	11/04/2004	EDM reflector tower	46.1735	-122.1606	1479.39
P702	PBO	11/05/2004	Shallow-drilled and braced	46.3002	-122.3456	1305.70
P690	PBO	02/01/2005	EDM reflector tower	46.1800	-122.1899	2078.91
P699	PBO	02/02/2005	EDM reflector tower	46.1898	-122.2032	2274.11
P689	PBO	10/23/2005	Shallow-drilled and braced	46.1896	-122.3606	1359.46
THAR	CVO	06/28/2006	EDM instrument tower	46.2753	-122.1740	1430.55
P701	PBO	09/22/2006	Shallow-drilled and braced	46.1946	-122.1333	1247.79
P694	PBO	09/24/2006	Shallow-drilled and braced	46.2996	-122.1819	1726.03
P692	PBO	09/25/2006	Shallow-drilled and braced	46.2245	-122.1842	1492.23
P700	PBO	09/26/2006	Shallow-drilled and braced	46.1781	-122.2173	1522.03
P691	PBO	09/29/2006	Shallow-drilled and braced	46.2315	-122.2269	1183.26
P703	PBO	09/30/2006	Shallow-drilled and braced	46.1453	-122.1963	988.75
P705	PBO	09/30/2006	Shallow-drilled and braced	46.1730	-122.3106	1151.23

files obtained from the Jet Propulsion Laboratory (Pasadena, Calif.). The methods described by Blewitt (1989) are applied to the daily solutions of a network of stations, which improves measurement precision by estimating carrier-phase ambiguities within overlapping subsets of stations. The resulting minimally constrained network solution is in the reference frame of the satellite orbits (a nonfiducial reference frame—for example, Helfin and others, 1992). The GPS data processing to this point is standardized by using gp, a set of UNIX scripts and programs developed by Will Prescott and others at the USGS in Menlo Park, Calif. (see http://quake.wr.usgs.gov/research/deformation/gps/gpmanual/index.html).

Transformation of Minimally Constrained Solution to a Terrestrial Reference Frame

The next step in the GPS data-reduction process is experimental and has changed over time. The daily, minimally constrained, fixed-ambiguity network solution is merged with a point-position solution of a global network of CGPS stations (http://quake.wr.usgs.gov/research/deformation/gps/auto/*Track/*) that are in the stable interiors of the Earth's lithospheric plates; their positions and velocities are defined in the ITRF2000 terrestrial reference frame (Altimimi and others, 2002). No ambiguity resolution is attempted for the global network because of the large station separations. Station positions in the ITRF2000 frame station evolve following the no-net-rotation NNR-NUVEL-1A model of DeMets and others (1994). We are interested in deformation relative to the North American plate (NOAM), and for this purpose we created a nominal fixed-NOAM ITRF2000 reference frame using the Euler vector for NOAM given by Altimimi and others (2002, their table 6). We refer herein to this reference frame as "fixed-NOAMgp."

The combined (global and local), minimally constrained daily solution is transformed into ITRF2000 and to the fixed-NOAMgp terrestrial reference system by applying a seven-parameter Helmert transformation (x,y,z translations + rotations about the three axes + a scale change) that minimizes the misfit in the observed positions of the global reference stations with the positions predicted for that day. Misfit residuals from this adjustment are examined automatically to identify outliers, a reference station is removed from the solution if its residual exceeds five times the expected error, and the transformation process is iterated. Finally, the minimally constrained network solution and the combined ITRF and nominal fixed-NOAMgp solutions are archived, and Web-accessible plots of station time series and estimates of station velocities are updated.

GPS Networks Near Mount St. Helens

Campaign GPS and CGPS data from stations near Mount St. Helens are included in three regional groupings (networks): Cascadia includes most regional CGPS stations in the Pacific Northwest; Helens includes Mount St. Helens campaign GPS stations along with a subset of the regional CGPS stations that are processed only on the days campaign GPS data are collected; and HelensMonit includes CGPS stations around Mount St. Helens, a few regional GPS stations, and campaign GPS stations that provide bedrock local ties to the Mount St. Helens CGPS stations (for example, see http://quake.wr.usgs.gov/research/deformation/gps/auto/Helens/). These regional groupings are arbitrary and have resulted from the combination of a rapid increase in the number of stations over time and from the computational efficiency of processing data from networks having a smaller number of stations. New analysis techniques that detect and remove common-mode error in the station positions are most successful when all Mount St. Helens and related reference-station data are processed in a single group.

Local Terrestrial Reference Frames

The precision of regional GPS solutions can be improved by removing spatially correlated noise (Wdowinski and others, 1997). The transformation to a terrestrial reference frame is approximate, and it can be refined by using local stations (within a few hundred kilometers) with well-defined positions and velocities to estimate common-mode daily bias in the local solutions. Common-mode daily bias is estimated by either stacking the position component residuals (after removal of linear trends) of the local reference stations or by the equivalent procedure of estimating origin translations of the daily network solutions. We estimate the local network translations from a subset of CGPS reference stations included in the solutions.

We construct a local reference frame for the Mount St. Helens region to define the position of selected CGPS reference stations at any given time. The reference stations have long measurement histories, daily position measurements, and constant velocities. Starting with the daily combined, fixed-NOAMgp solutions, we remove all but the local reference stations and a subset of NOAM global stations. These solutions are merged to produce weekly averages of positions, outliers are identified and removed, and then the weekly averages for multiple years are adjusted to give an average position at a particular time and average station velocities (see Smith and others, 2004). We include the subset of ITRF2000 NOAM stations to keep the local reference frame aligned with our fixed-NOAMgp reference frame during the adjustment. Thereafter, most NOAM stations are removed from the final local reference frame because they are far from the region of interest.

The daily local solutions, which include several of the local reference stations, are then shifted into the local reference frame by applying a three-parameter Helmert transformation (3D translation), which minimizes the misfit between the observed positions of the local reference stations and those predicted by the local reference frame for that date. Occasionally, one or more of the local reference stations is poorly fit; it is removed from the regional solution and the transformation is iterated.

Removing the common-mode daily bias in the solutions can reduce the scatter in the station-component time series by a factor of 2 to 3 (Williams and others, 2004). Local-station seasonal wander, data offsets, and nonlinear deformation remain in the station-component time series after removing spatially correlated noise common to the reference stations. We use the QOCA (pronounced "coca") software (Quasi-Observation Combination Analysis) (Dong and others, 1998, 2002, 2006), designed and developed at NASA's Jet Propulsion Laboratory, for final analysis of the trends and noise in the GPS solutions. The QOCA software can be used to align the minimally constrained network solutions to any defined terrestrial reference frame, manipulate 3D station-position time series, and calculate spatial and temporal deformation.

Deformation in the Mount St. Helens Region Determined by Using GPS and Trilateration Survey Data

Tectonic interactions between the Pacific, Juan de Fuca, and North American plates displace and deform the ground in the Pacific Northwest (for example, Savage and others, 1991; Murray and Lisowski, 2000; McCaffrey and other, 2000; Savage and others, 2000; Miller and others, 2001; Svarc and others, 2002; Mazzotti and others, 2003). The widespread secular tectonic deformation can mask the more localized background and episodic deformation across the volcanic arc. For example, locking of the shallow interface between the Juan de Fuca and North American plates compresses the adjacent coastal region of the North American plate in the east-northeast direction of relative convergence between the plates. More enigmatic are the rigid-body movements of large continental regions (microplates) and possible strain accumulation or relative motion along their boundaries (for example, Wells and others, 1998; Wells and Simpson, 2001).

We use repeated GPS surveys and data from CGPS stations to derive a model for background tectonic deformation in the Mount St. Helens region. We then compare the modeled background rates of strain accumulation with that determined from line-length changes in an arc-crossing, regional trilateration network that was measured in 1982, 1991, and 2000. Finally, the tectonic model is used to adjust observed GPS station movements to determine the rate and pattern of volcanic deformation around Mount St. Helens since 2000.

Tectonic Rigid-Body Rotation and Strain Accumulation in the Mount St. Helens Region

The Helens GPS network includes several regional campaign stations with well-determined velocities, some occupied as early as 1992 (stations marked with yellow triangles in figs. 2 and 3). In addition, solutions for the Helens and Cascadia networks include several PANGA CGPS stations with well-determined velocities that are situated in the arc and back-arc regions (stations with blue names in figs. 2 and 3).

The GPS station velocities in the fixed-NOAMgp terrestrial reference frame reveal what appears to be a regional, clockwise, rigid-block rotation (figs. 2, 3). This microplate motion is roughly consistent with paleomagnetic studies that suggest widespread Cenozoic rotation in the Cascadia forearc (for example, Simpson and Cox, 1977; Magill and others, 1982; Wells and others, 1998) and is similar to widespread block rotation observed by using GPS to survey much of the Cascadia forearc, arc, and backarc region (McCaffrey and other, 2000; Savage and others, 2000; Svarc and other, 2002). In addition to the obvious block rotation, there may be a small amount of internal deformation (strain accumulation).

We use the method of Savage and others (2001, their appendix A) to simultaneously estimate an Euler vector for the rigid-body rotation and the rate of strain accumulation that best fits the observed regional-station velocities. Our best-fitting tectonic model was obtained by excluding the northern PANGA CGPS stations (CHWK, DRAO, SEDR, BREW) from the model. The resulting Euler vector, principal strain rates, and predicted station velocities are shown in figure 3 and summarized in table 2 (Helens GPS). An independent estimate of the rotation rate and strain was computed using QOCA, which gave similar results (table 2, Helens GPS QOCA). The computed Euler vector is roughly consistent with previous studies of GPS-measured deformation in Cascadia, which show a similar rate of clockwise block rotation (McCaffrey and other, 2000; Savage and others, 2000; Svarc and others, 2002). A small amount of uniaxial contraction (–18.0±1.9 nanostrain/yr, extension reckoned positive) accumulates in the ~N. 60° E. direction of relative convergence between the Juan de Fuca and North American plates. This rate of strain accumulation is equivalent to an average of 3.6 mm/yr of east-northeast-directed contraction across the 200-km-wide zone covered by the regional GPS stations and likely represents penetration of deformation from the locked subduction thrust into this region. The tectonic model does not define possible background vertical deformation, and we assume that there is none because regional studies of historical leveling data show little long-term elevation change across the Cascades (Verdonck, 2006).

Deformation in the 1980s and 1990s Within a Regional High-Precision Trilateration Network

The Helen trilateration network, which straddles the Cascade volcanic arc in southwestern Washington, was established to track regional strain accumulation following the 1980 crater-forming eruption of Mount St. Helens (fig. 4). Line lengths were measured in 1982 and 1991, and they were recovered with GPS in 2000 (EDM-measured line lengths can be downloaded from http://quake.wr.usgs.gov/research/deformation/gps/geodolite/index.html). The GPS-recovered line lengths were corrected for the –0.283 ppm systematic scale bias relative to Geodolite line lengths derived empirically by Savage and others (1996).

Table 2. EDM and GPS network strain and rotation rates.

[Strain rates within entire network assuming uniform strain accumulation. --, data not calculated.]

Network	Averaging interval	ε_1 (nano-strain/yr)	ε_2 (nano-strain /yr)	Azimuth ε_3 (degrees clockwise from north)	Rotation rate (nanoradian/yr)	Euler Pole latitude (degrees)	Euler Pole longitude (degrees)	Correlation latitude-longitude	Standard deviation unit weight
Helens EDM	1982.7–1991.7	82±28	62±27	44 ± 37	--	--	--	--	--
Helens EDM	1991.7–2000.7	11±29	–10±29	70 ± 35	--	--	--	--	--
Helens GPS	1992–2004	2.5±1.7	–18.0±1.9	63.8 ± 3.5	–15.4±1.2	44.476±0.141	–118.526±0.252	–0.804	1.0
Helens GPS (QOCA)	1992–2004	–0.8±2.7	–20.1±2.9	55.0 ± 6.0	–14.3±2.0	45.969±0.31	–117.876±0.540	–0.932	0.84

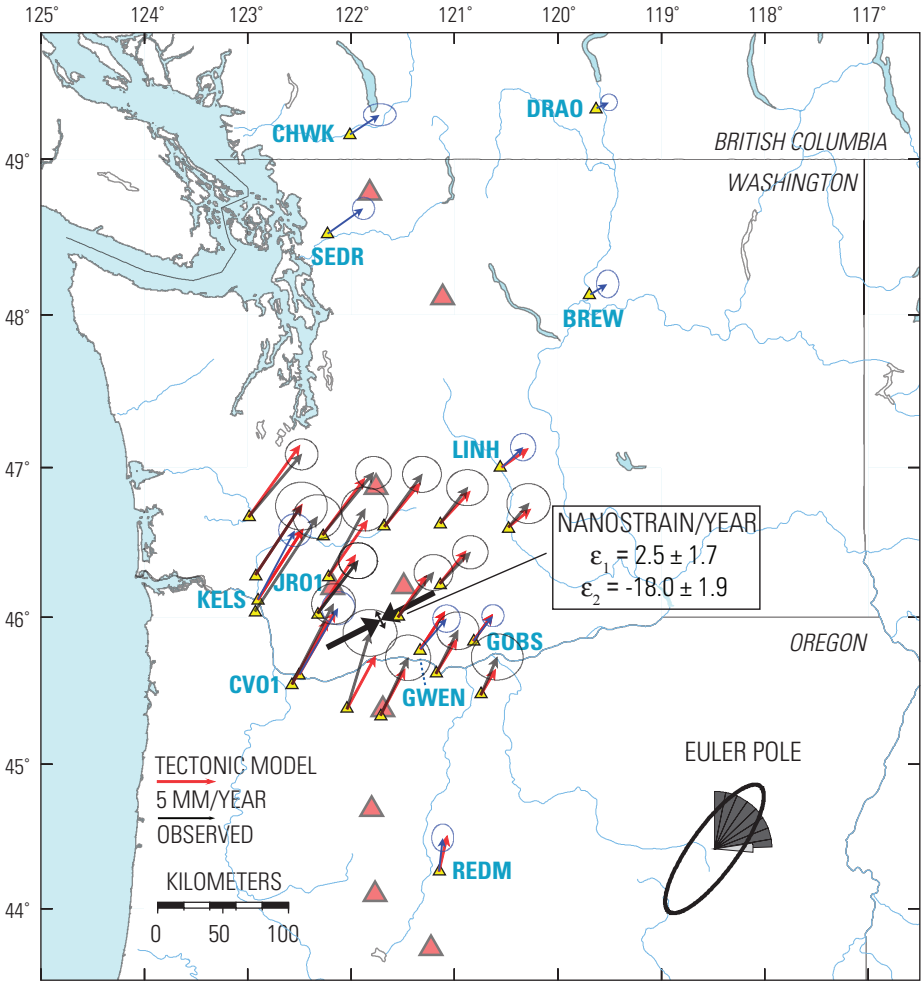

Figure 3. Map of GPS station velocities in Oregon, Washington, and British Columbia used to define the tectonic model of background rigid-block rotation and uniform strain accumulation. Observed station velocity vectors (black or blue arrows tipped with 95-percent-confidence error ellipses) are relative to stable North America. Velocity vectors predicted using the model are shown in red. Region for 95-percent confidence of the computed Euler pole is indicated by dark ellipse in eastern Oregon, rotation rate is indicated by dark wedges, and one-standard-deviation uncertainty in rotation rate is indicated by a light wedge. Large black arrows represent computed directions and rates of principal strains. The four most northerly CGPS stations (CHWK, DRAO, SEDR, BREW) are not included in the tectonic model calculation. Large orange triangles mark locations of major Cascade Range volcanoes.

Line lengths increased consistently by 1 to 3 cm between 1982 and 1991 but showed no significant change between 1991 and 2000. The uncertainty in a Helen line length measured with a Geodolite is between 4 and 8 mm, with the larger value for the longest lines in the network (see Savage and Prescott, 1973). By converting the observed line-length changes to extension rates and assuming that strain accumulates uniformly over the network, we can map variation in the extension rates as a function of line azimuth into surface tensor-strain-rate components. Between 1982 and 1991, areal dilatation ($\varepsilon_1 + \varepsilon_2$, where ε_1 and ε_2 are the principal strains and extension is reckoned positive) accumulated at a rate of 144±39 nanostrain/yr, which is equivalent to a ~3 mm/yr (~70 nanostrain/yr) average increase in the length across the ~40-km-aperture network in any direction. This rate of strain accumulation is distinctly different than the background areal dilatation rate (at –15±3 nanostrain/yr) estimated with the tectonic model (table 2 – note areal dilatation = $\varepsilon_1 + \varepsilon_2$). No significant strain accumulated between 1991 and 2000.

Surficial areal dilatation is expected to accompany recharge of a deep spheroidal magma reservoir. Areal dilatation is also a sensitive measure of possible systematic scale error in the individual EDM surveys because such error is proportional to distance measured and is independent of the direction of the line (Savage and others, 1986, p. 7471–7472). Systematic error in Geodolite line-length measurements is estimated to contribute about 0.14 ppm to the error in a line length, whereas a total systematic error of about 0.6 ppm between the two surveys is needed to reproduce the observed dilatation. The contribution of possible systematic error is included in the uncertainty in the rate of areal dilatation, and we conclude that the observed areal dilatation between 1982 and 1991 is too large for systematic error alone. Some other phenomenon, like recharge of the magma reservoir, contributes to this deformation.

Deformation in the Mount St. Helens GPS Network in the Years before September 23, 2004

The 43-station Helens campaign GPS network, surveyed in 2000 and 2003, extends for more than 50 km around Mount

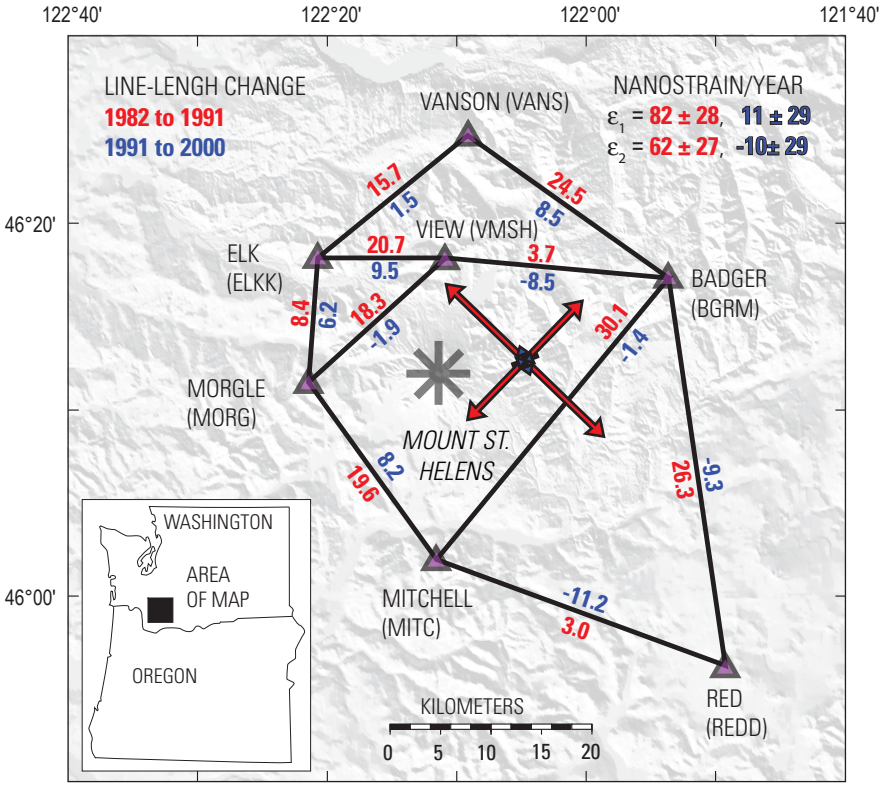

Figure 4. Map of the Helen trilateration network. Measured length changes and calculated uniform principal strain rates from 1982 to 1991 are shown in red. Corresponding values from 1991 to 2000 are shown in blue. EDM station names are given, with four-character GPS station name in parentheses. Line lengths in 2000 were measured with GPS. Directions and relative magnitudes of principal strain rates are shown with large arrows; their values are given in nanostrain per year.

St. Helens (stations marked with red triangles in fig. 2). Network coverage is increased in space and time by incorporating surveys of 13 nearby campaign GPS stations, some of which were measured as early as 1992, in the QOCA adjustment for average station velocities. Several PANGA CGPS stations, most in service since 1997 (table 1), are included in the solutions, and one of these, JRO1, is 9 km north of Mount St. Helens.

We use the predictions of the tectonic model given in table 2 (network Helens GPS) to remove regional secular deformation from the computed average GPS station velocities. We did not propagate uncertainty in the tectonic model into error in the corrected station velocities shown in figure 5 and listed in table 3. At the stations with well-defined velocities—those stations included in the tectonic-model calculation (stations marked with yellow triangles in fig. 5)—we see no significant motion. A few stations near Mount St. Helens have significant velocities, but their movements lack a consistent pattern, so we suspect they result from local instabilities or survey errors.

Examining the station velocities in the local network around Mount St. Helens (fig. 6), we observe no consistent pattern of deformation, but roughly half of the velocities exceed the 95-percent-confidence error ellipses. The highest velocity is found in the crater at station DMSH on the September 1984 lobe of the old dome, which moves to the east-northeast and down. This lobe is west of the old dome's center, and the observed motion is toward the center of the old dome, consistent with the motion expected as the old dome continues to cool and shrink. The westward velocity of stations MORG and WGOT, west of Mount St. Helens, is greater than 5 mm/yr, but other nearby stations show little or no significant motion. With surveys only in 2000 and 2003, it is difficult eliminate local instabilities or survey error, such as instrument setup, as a cause for the anomalous velocities. The daily measurements of position change at CGPS station JRO1 provide the strongest evidence for the lack of anomalous deformation in the years before September 2004. We examine the JRO1 data in the next section.

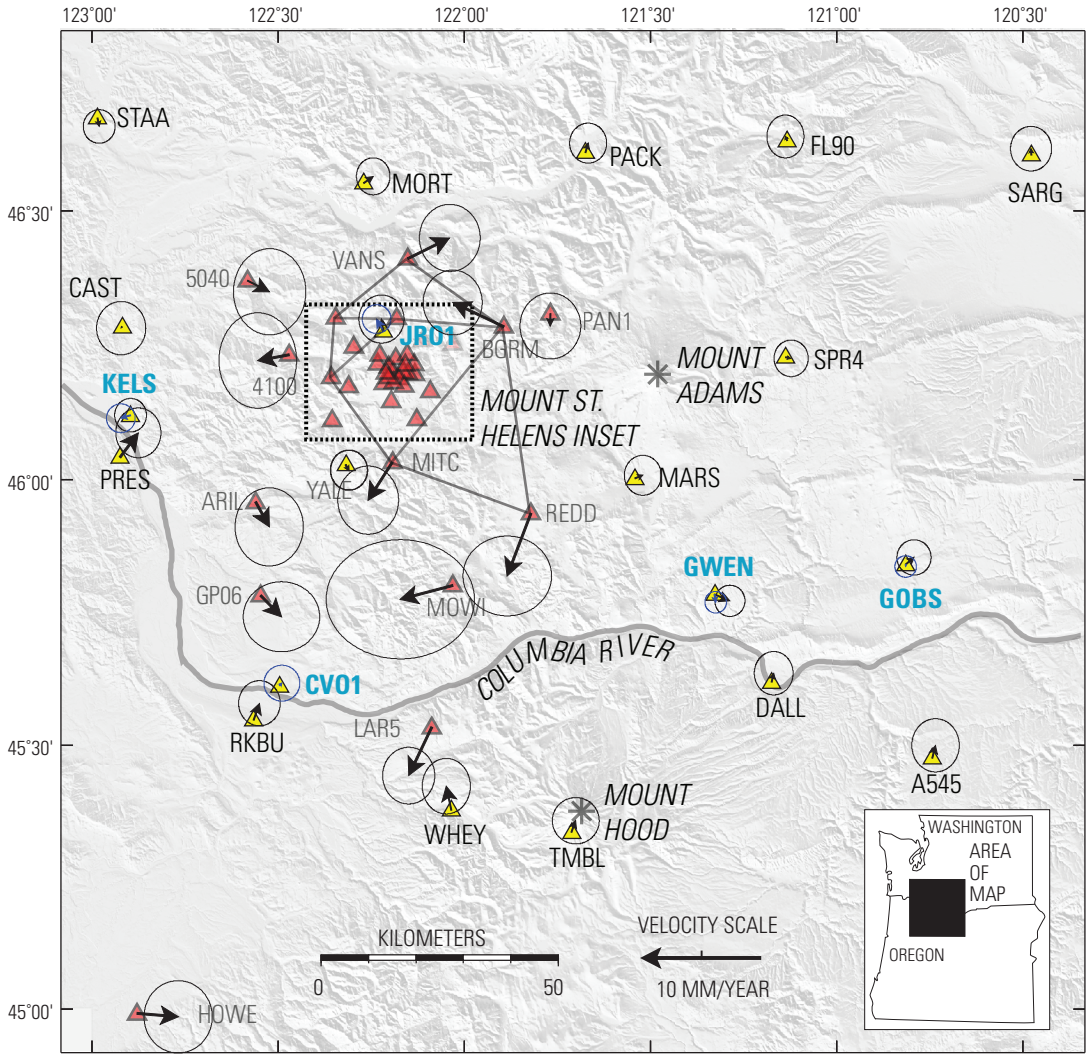

Figure 5. Map showing average GPS station horizontal-velocity vectors (tipped with 95-percent-confidence error ellipses, scale at bottom) for southwest Washington and northwest Oregon through September 2004, corrected for background motion predicted by a tectonic model. None of stations marked with yellow triangles, which were included in calculations for the tectonic model, have significant residual velocity. CGPS station names and velocity vectors are shown in blue. Most stations indicated with red triangles were surveyed only in the summers of 2000 and 2003.

Table 3. Adjusted Helens campaign GPS network average station velocities through September 23, 2004.

[Velocities are in nominal ITRF2000 fixed North American Plate terrestrial reference frame and are corrected for regional rigid-body rotation and strain.]

Station	Longitude (degrees)	Latitude (degrees)	East velocity ± 1σ error (mm/yr)	North velocity ± 1σ error (mm/yr)	E-N correlation	Up velocity ± 1σ error (mm/yr)
4100	-122.4706	46.2316	-2.65 ± 1.34	-0.50 ± 1.65	-0.04	-0.49 ± 6.64
5040	-122.5819	46.3695	1.86 ± 1.25	-0.95 ± 1.49	-0.06	13.87 ± 5.70
A545	-120.7435	45.4745	0.27 ± 0.82	1.08 ± 0.92	0.01	-1.76 ± 3.60
APEC	-122.1330	46.1950	-1.92 ± 1.06	4.00 ± 1.13	-0.01	-1.77 ± 4.93
ARIL	-122.5608	45.9561	1.16 ± 1.18	-2.10 ± 1.35	-0.05	4.29 ± 5.47
BGRM	-121.8943	46.2834	-4.32 ± 1.02	2.05 ± 1.12	0.00	0.14 ± 4.66
BIVO	-122.1962	46.1453	-2.37 ± 1.20	-4.60 ± 1.41	-0.03	11.24 ± 5.63
CAFE	-122.1349	46.2135	-2.56 ± 1.08	-0.39 ± 1.17	-0.03	0.36 ± 5.05
CANN	-123.9603	45.8617	4.29 ± 0.72	0.11 ± 0.77	-0.04	-0.94 ± 2.93
CAST	-122.9188	46.2833	-0.09 ± 0.85	-0.11 ± 0.92	-0.08	3.42 ± 3.30
CVO1	-122.4961	45.6109	-10.76 ± 6.44	1.92 ± 7.12	0.00	17.10 ± 29.68
DALL	-121.1752	45.6178	0.18 ± 0.67	0.76 ± 0.75	0.00	-3.40 ± 2.81
DMSH	-122.1910	46.2000	27.69 ± 1.04	9.39 ± 1.15	-0.01	-90.29 ± 4.86
DRAO	-119.6250	49.3226	-1.78 ± 0.43	1.46 ± 0.44	0.00	1.25 ± 1.39
EADM	-122.1521	46.1973	-1.18 ± 1.04	0.90 ± 1.12	-0.02	-3.54 ± 4.84
ELKK	-122.3452	46.3009	-0.65 ± 1.09	0.94 ± 1.18	-0.02	-0.24 ± 4.95
FL90	-121.1333	46.6288	-0.14 ± 0.64	0.36 ± 0.74	0.05	-6.53 ± 2.90
GOBS	-120.8147	45.8388	0.69 ± 0.59	0.61 ± 0.61	-0.02	0.33 ± 1.68
GP06	-122.5472	45.7810	1.76 ± 1.32	-1.80 ± 1.21	0.06	-5.07 ± 4.49
GWEN	-121.3276	45.7826	1.28 ± 0.52	-0.53 ± 0.54	-0.02	0.51 ± 1.58
HOWE	-122.8797	44.9900	3.50 ± 1.18	-0.29 ± 1.25	-0.07	-4.69 ± 4.57
HPAD	-122.0315	46.2520	-4.97 ± 1.03	1.09 ± 1.16	0.00	2.94 ± 4.70
JARD	-122.2973	46.2469	-1.89 ± 1.10	0.71 ± 1.19	-0.01	-28.35 ± 5.13
JRO1	-122.2176	46.2751	-0.16 ± 0.78	1.03 ± 0.83	-0.01	-2.93 ± 3.53
KELS	-122.8961	46.1182	-0.01 ± 0.55	0.02 ± 0.58	-0.02	-0.05 ± 1.64
LAR5	-122.0876	45.5327	-1.95 ± 0.90	-4.10 ± 0.98	-0.01	-1.77 ± 3.96
LOOW	-122.1843	46.2248	4.03 ± 1.05	0.77 ± 1.13	-0.01	1.29 ± 4.88
LVCY	-122.0912	46.1638	3.52 ± 3.69	2.02 ± 2.82	0.11	2.91 ± 8.44
MARS	-121.5419	46.0001	0.66 ± 0.64	0.28 ± 0.69	-0.02	1.29 ± 2.72
MITC	-122.1931	46.0309	-2.05 ± 1.05	-3.21 ± 1.18	-0.01	4.56 ± 4.73
MORG	-122.3572	46.1893	-7.42 ± 1.00	2.70 ± 1.11	-0.01	-0.66 ± 4.61
MORT	-122.2704	46.5506	0.80 ± 0.58	0.56 ± 0.64	-0.01	-1.76 ± 2.51
MOWI	-122.0308	45.7998	-4.45 ± 2.56	-1.17 ± 2.06	-0.12	-0.15 ± 6.61
NEBU	-122.2173	46.1782	-3.56 ± 1.08	2.41 ± 1.17	0.01	3.49 ± 5.02
NELR	-122.1649	46.1993	-1.33 ± 1.06	-1.07 ± 1.13	-0.03	1.99 ± 4.88
NESK	-123.9662	45.1343	5.07 ± 0.79	1.86 ± 0.83	-0.05	-1.51 ± 3.10
NMAR	-122.1280	46.1112	-1.23 ± 1.06	0.81 ± 1.20	0.03	5.58 ± 4.87

Table 3. Adjusted Helens campaign GPS network average station velocities through September 23, 2004. —Continued

[Velocities are in nominal ITRF2000 fixed North American Plate terrestrial reference frame and are corrected for regional rigid-body rotation and strain.]

Station	Longitude (degrees)	Latitude (degrees)	East velocity ± 1σ error (mm/yr)	North velocity ± 1σ error (mm/yr)	E-N correlation	Up velocity ± 1σ error (mm/yr)
NWDO	-122.2037	46.2096	2.72 ± 1.04	0.10 ± 1.13	-0.01	0.95 ± 4.79
PACK	-121.6752	46.6068	0.23 ± 0.64	0.80 ± 0.69	0.00	-5.60 ± 2.71
PAN1	-121.7685	46.3078	-0.02 ± 1.05	-1.04 ± 1.14	0.00	0.22 ± 4.84
PRES	-122.9245	46.0401	1.54 ± 0.78	2.06 ± 0.86	-0.04	-4.45 ± 3.23
R100	-122.1538	46.2322	1.16 ± 1.01	-1.01 ± 1.12	0.00	-0.64 ± 4.60
REDD	-121.8210	45.9349	-2.01 ± 1.53	-5.29 ± 1.38	-0.04	15.11 ± 5.71
RKBU	-122.5660	45.5467	0.49 ± 0.72	1.41 ± 0.78	-0.03	-5.58 ± 2.96
RS26	-123.4611	45.7968	3.37 ± 0.84	1.31 ± 0.94	-0.04	-2.90 ± 3.46
SARG	-120.4772	46.6024	-0.04 ± 0.71	0.53 ± 0.77	-0.01	-1.67 ± 2.83
SERI	-122.1765	46.1877	-2.81 ± 1.10	-4.41 ± 1.22	-0.05	-5.52 ± 5.07
SESL	-122.1615	46.1737	-1.37 ± 1.06	1.71 ± 1.14	-0.02	0.40 ± 4.94
SMCR	-122.1117	46.2586	-3.83 ± 0.96	2.37 ± 1.05	0.00	0.78 ± 4.33
SOFO	-122.2329	46.2153	0.83 ± 1.09	5.43 ± 1.18	-0.01	-1.88 ± 5.04
SPR4	-121.1371	46.2269	0.46 ± 0.59	-0.11 ± 0.63	-0.02	0.52 ± 2.47
SRID	-122.1899	46.1801	-1.65 ± 1.03	0.36 ± 1.12	-0.01	-5.21 ± 4.78
STAA	-122.9853	46.6708	0.15 ± 0.55	-0.72 ± 0.58	-0.03	1.60 ± 2.33
STUD	-122.2269	46.2314	2.99 ± 1.08	1.89 ± 1.18	0.00	-0.12 ± 5.03
TMBL	-121.7119	45.3340	0.35 ± 0.81	0.98 ± 0.80	-0.07	0.85 ± 3.22
TUBE	-122.3547	46.1095	2.22 ± 1.25	3.59 ± 1.41	-0.06	-2.24 ± 5.88
VANS	-122.1516	46.4101	3.54 ± 1.05	1.75 ± 1.16	0.01	0.47 ± 4.77
VMSH	-122.1820	46.2998	-1.54 ± 1.04	3.07 ± 1.12	-0.01	2.91 ± 4.81
WGOT	-122.3106	46.1730	-8.49 ± 0.88	0.80 ± 0.97	-0.01	-4.27 ± 3.94
WHEY	-122.0349	45.3762	-0.43 ± 0.83	2.02 ± 0.96	0.03	-4.67 ± 3.69
WIWE	-122.1587	46.2129	1.20 ± 1.05	-4.18 ± 1.13	0.00	2.21 ± 4.85
WRAD	-122.2035	46.1897	0.25 ± 1.07	7.46 ± 1.18	0.02	3.44 ± 5.00
WRID	-122.2107	46.1978	1.05 ± 1.05	-2.31 ± 1.13	0.00	0.23 ± 4.87
YALE	-122.3181	46.0262	0.26 ± 0.64	-0.47 ± 0.69	-0.07	1.18 ± 2.61

Time Series of Deformation from CGPS Data Collected at Johnston Ridge Observatory

A detailed history of deformation near Mount St. Helens since 1997 is found in the daily displacement components of CGPS station JRO1. The Cascadia network includes daily solutions in the fixed-NOAMgp reference frame and in a local reference frame that is defined by a subset of 11 CGPS stations in the network (table 4). QOCA's time-series analysis is used to simultaneously compute the component velocities, offsets, and repetitive seasonal displacements of JRO1. We do not include the anomalous data after September 23, 2004, in this analysis for background deformation. Outliers in the time series, found mainly in the winter when ice and snow accumulate around the GPS antenna, are defined as observations where the residual east or north displacement is larger than 5 mm, and the residual vertical displacement is larger than 15 mm. These residual outliers are about three times the weighted root-mean-square (WRMS) scatter observed in the JRO1 time-series analysis (table 4). Of the 2,267 daily observations, 130 (6 percent) were removed from the analysis because one or more of the components was identified as an outlier.

Small vertical offsets (~13 mm) in the time series were introduced on July 8, 1998, when a UNAVCO radome replaced the original Snow radome, and on July 16, 2002, when a SCIGN radome replaced the UNAVCO radome. The vertical offsets are calculated in QOCA by first setting assumed offset values based on estimates from a short span of data around the offset (we use 0.2 year), which is then given a weight of 0.25 times the offset; the final values are estimated simultaneously with other parameters. In our final analysis, only vertical offsets are estimated because initial analysis resulted in horizontal offsets that were small and insignificant. Nevertheless, the long-term trends could be biased slightly by error in the applied vertical offsets and possible small, horizontal offsets related to the antenna-radome changes.

The estimated JRO1 component velocities, offsets, and repetitive seasonal movements are removed to produce a resid-

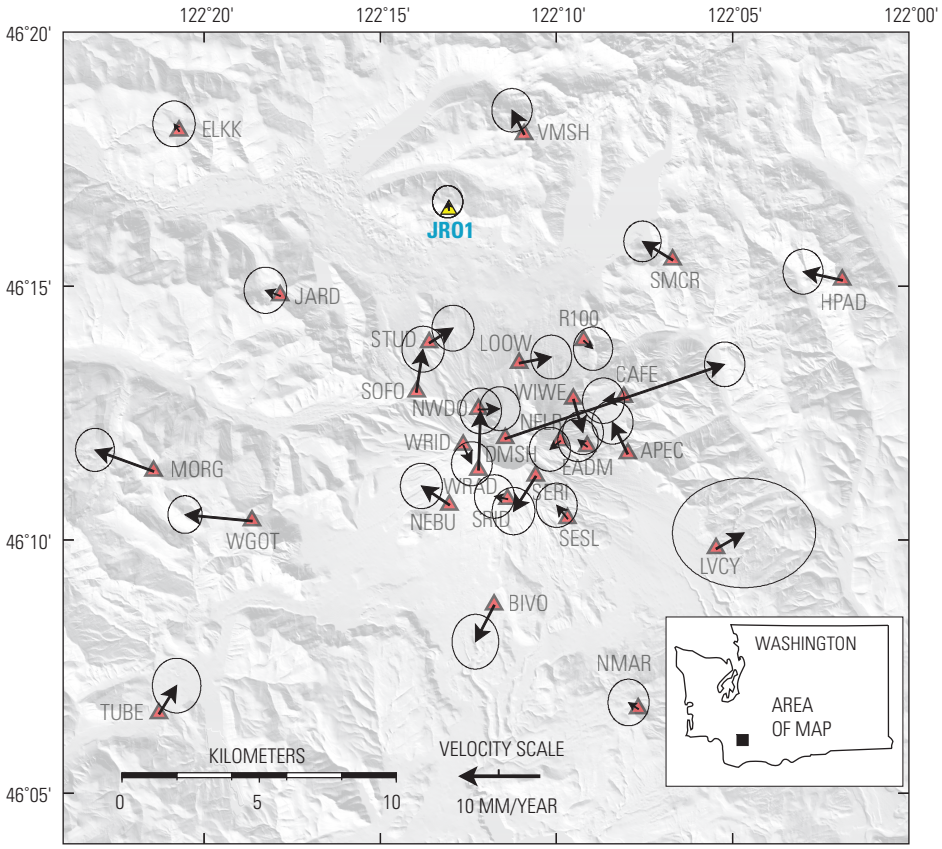

Figure 6. Map showing 2000–2003 corrected average GPS station horizontal-velocity vectors (tipped with 95-percent-confidence error ellipses, scale at bottom) for Mount St. Helens area. Although many stations show significant velocities, there is no systematic pattern that might suggest premonitory deformation before the start of the 2004 eruption. GPS station DMSH, on the 1980–86 lava dome, moved downward 87 mm/yr and east-northeastward 35 mm/yr, presumably as a result of cooling and compaction of the dome.

Table 4. Time-series analysis of Cascadia network local reference frame stations.

[WRMS is weighted root-mean-squared deviation (experimental standard deviation). Phases are relative to start of the calendar year. Data for station KELS are divided into two intervals to calculate velocities; other KELS data, equivalent between columns, are shown by dashes in second KELS column.]

Station	JRO1	KELS	KELS	BREW	CVO1	GOBS	REDM
Start date (year month day)	19970523	19971010	20040923	19971010	20030104	19970827	19980725
End date (year month day)	20040922	20040922	20061013	20061013	20061013	20061013	20061013
Number of daily positions (post-1996)	2,137	2,977	--	1,669	1,308	3,149	2,889
Number of outliers	130	201	--	1	4	30	31
East WRMS (mm)	1.70	1.62	--	0.82	1.13	1.13	1.32
North WRMS (mm)	1.75	1.77	--	0.91	1.19	1.23	1.12
Up WRMS (mm)	5.01	4.62	--	3.23	3.50	3.36	3.25
East velocity (mm/yr)	2.76	3.07	6.14	1.33	3.26	1.52	0.16
North velocity (mm/yr)	5.82	5.84	5.03	0.75	5.63	2.09	2.80
Vertical velocity (mm/yr)	-1.99	-0.45	0.11	0.18	-1.54	-0.73	0.02
East annual amplitude (mm)	2.02	0.84	--	0.35	0.51	1.83	0.35
East annual phase (degrees)	52.35	37.32	--	239.69	288.89	139.06	351.70
North annual amplitude (mm)	1.96	0.98	--	0.10	0.06	1.30	0.62
North annual phase (degrees)	137.86	160.71	--	39.96	161.07	326.93	144.47
Vertical annual amplitude (mm)	1.70	1.10	--	0.35	1.66	0.49	0.97
Vertical annual phase (degrees)	25.41	354.79	--	284.29	356.08	277.76	50.14
East semiannual amplitude (mm)	0.34	0.34	--	0.06	0.12	0.25	0.20
East semiannual phase (degrees)	244.99	109.28	--	316.72	176.88	267.05	220.03
North semiannual amplitude (mm)	0.80	0.22	--	0.11	0.19	0.30	0.27
North semiannual phase (degrees)	263.56	236.34	--	199.17	87.40	85.48	330.50
Vertical semiannual amplitude (mm)	0.64	0.31	--	0.01	0.84	0.40	0.19
Vertical semiannual phase (degrees)	276.03	122.27	--	22.97	84.91	140.26	145.93

Station	LIND	LINH	GWEN	DRAO	CHWK	SEDR
Start date (year month day)	19980728	20020506	19970827	19970827	19981119	19971007
End date (year month day)	20061013	20061013	20061013	20061013	20061013	20061013
Number of daily positions (post 1996)	1,145	1,531	3,138	3,255	2,543	3,209
Number of outliers	13	16	72	12	11	7
East WRMS (mm)	1.3	1.11	1.55	1.00	1.10	1.14
North WRMS (mm)	1.19	1.15	1.50	1.16	1.42	1.33
Up WRMS (mm)	3.95	3.90	4.32	2.97	4.24	3.55
East velocity (mm/yr)	1.70	1.70	2.10	0.93	2.43	2.97
North velocity (mm/yr)	1.69	1.63	2.56	0.41	1.60	2.11
Vertical velocity (mm/yr)	-0.53	0.01	-0.85	1.61	0.25	-0.23
East annual amplitude (mm)	0.26	0.33	0.87	0.42	0.44	0.46
East annual phase (degrees)	90.92	75.29	278.58	73.03	322.68	305.77
North annual amplitude (mm)	0.81	0.48	0.39	0.24	0.37	0.23
North annual phase (degrees)	218.14	209.76	138.47	258.20	85.11	204.89
Vertical annual amplitude (mm)	0.47	1.64	1.69	0.71	0.47	0.09
Vertical annual phase (degrees)	83.08	25.46	229.45	98.87	160.64	279.40
East semiannual amplitude (mm)	0.11	0.37	0.15	0.12	0.02	0.28
East semiannual phase (degrees)	137.32	45.34	349.51	250.97	149.82	77.91
North semiannual amplitude (mm)	0.05	0.25	0.26	0.03	0.17	0.11
North semiannual phase (degrees)	306.59	269.95	232.06	278.87	168.30	30.14
Vertical semiannual amplitude (mm)	0.39	1.33	0.62	0.13	0.61	0.05
Vertical semiannual phase (degrees)	115.22	186.33	357.05	18.87	252.14	117.52

ual-component time series. The horizontal components are then rotated so that one component represents motion radial (N. 13.5° W.), and the other component represents tangential motion (N. 76.5° E.) to Mount St. Helens (fig. 7*A*). Previously identified outliers are included in these plots, but they will be outside the 5-mm (horizontal) and 15-mm (vertical) data-rejection criteria indicated by the yellow bands on figure 7.

Station JRO1 moved at the background rate (no slope in fig. 7*A*) until the start of unrest on September 23, 2004, when anomalous subsidence and movement toward Mount St. Helens began at the station. Intervals of low-level systematic noise remain in the residual-component time series, as do short periods of drift when winter snow and ice accumulate on the GPS antenna and distort its phase center.

The average velocity of station JRO1 derived from the time-series analysis is similar to the velocity estimated from the local reference-frame calculation, but it is 0.9 mm/yr faster in the north component and 0.5 mm/yr slower in the east component than the velocity predicted by the tectonic model. We later use the tectonic model to correct post-September 23, 2004, velocities at JRO1 and at other stations around Mount St. Helens having unknown secular velocities. The observed

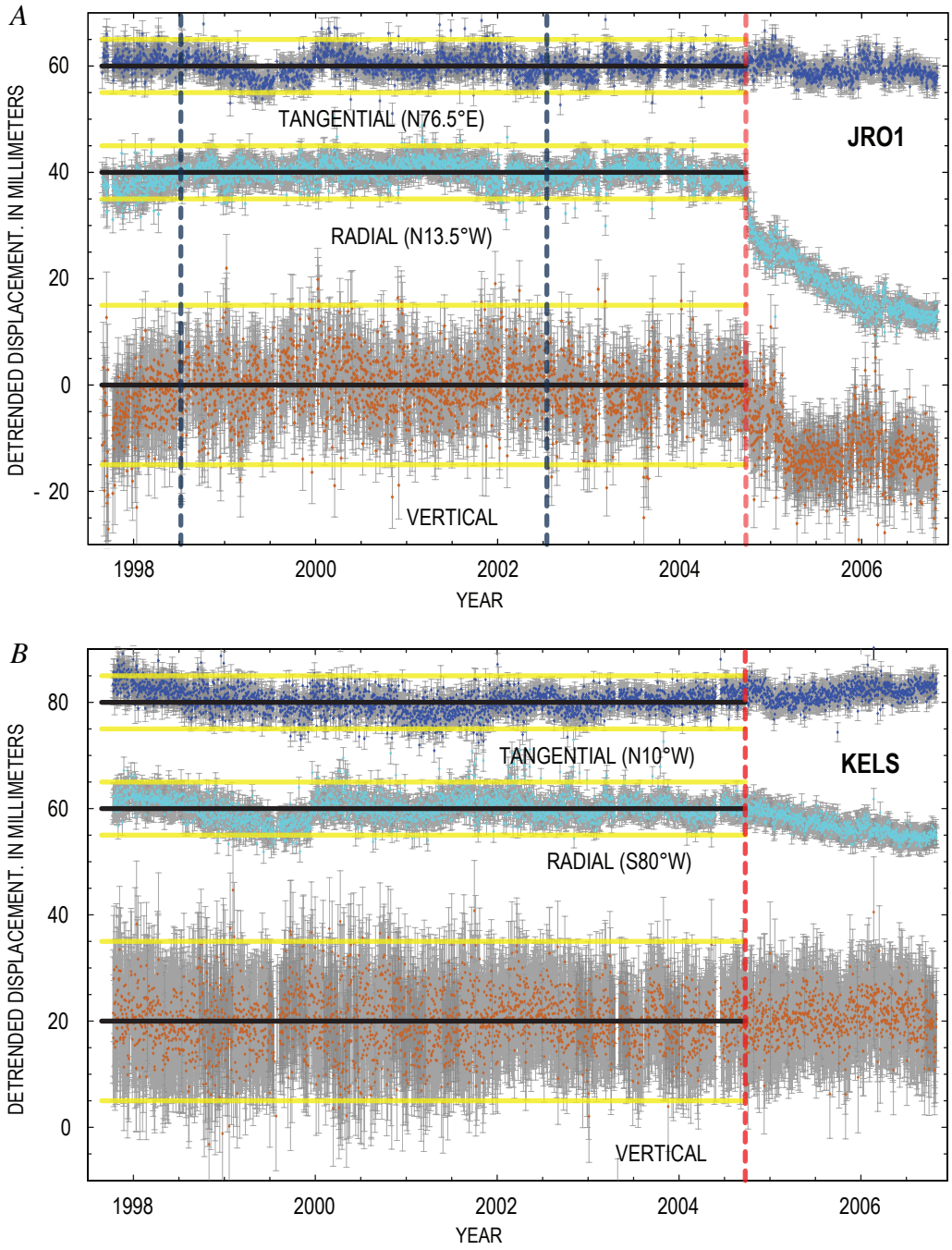

Figure 7. Stacked plots of detrended tangential, radial, and vertical daily average displacement of CGPS stations (*A*) JRO1, located 9 km north-northwest of Mount St. Helens, and (*B*) KELS, located 50 km west-southwest. Displacements are residuals from fitting a station velocity, mean value, cyclical annual and semiannual drift, and offsets from GPS antenna changes as determined by data collected through September 23, 2004. Vertical blue lines mark times that GPS antenna radomes were changed; vertical red line marks start of seismic unrest on September 23, 2004. Yellow horizontal lines are ±5 mm from pre-event tangential and radial mean values (outlier rejection limit) and ±15 mm from pre-event vertical mean value (outlier rejection limit). For station JRO1, one or more displacements were rejected for 130 of a total 2,267 days of data before September 23, 2004. For station KELS, one or more displacement components were rejected for 201 of 2,927 days of data.

discrepancy between the tectonic model and the observed motion at JRO1 is considered in the discussion of eruption-related deformation source models.

A small inward displacement of KELS, one of the PANGA CGPS stations used as a reference station in the local frame, also appears to have initiated at the start of volcanic unrest (fig. 7*B*). Station KELS is in Kelso, Wash., about 50 km west-southwest of Mount St. Helens, and the GPS antenna is mounted on a stable, deep-drilled, braced monument (Langbein and others, 1995) that is anchored at a depth of 10 m and isolated from the topsoil. The time-series analysis at KELS includes an additional term to resolve average velocities for the periods before and after September 23, 2004 (table 4). If deformation from the eruption of Mount St. Helens penetrated as far as station KELS, then it likely is the result of magma chamber pressure changes in a relatively deep (~10 km) source. We later examine data from several PBO CGPS stations located an equivalent distance to the north of Mount St. Helens to determine whether eruption-related deformation could be detected there.

GPS Station Displacements Early in the 2004–2006 Eruption

The only direct measure of deformation associated with the initiation of the eruption was made at JRO1, where slow, relatively steady motion toward Mount St. Helens was observed (fig. 8). The movement of station JRO1 was fastest in the two weeks after September 23, 2004, but even then it averaged only about 0.5 mm/day (inset, fig. 8). The inward movement continued at a nearly linear rate until a few days after the vigorous steam-and-ash explosion on October 5, 2004, when movement began to slow at a time-decaying rate. We later conclude that deformation has gradually slowed at other CGPS stations around Mount St. Helens.

The conduit that fed the eruptions in the 1980s is buried under the dome that developed in the years after the crater formed and that presumably was plugged with cooled magma. Was this plug pushed out at the start of the new dome-building eruption or was it bypassed? If a bypass formed, most likely it would appear as a dike that propagated to the

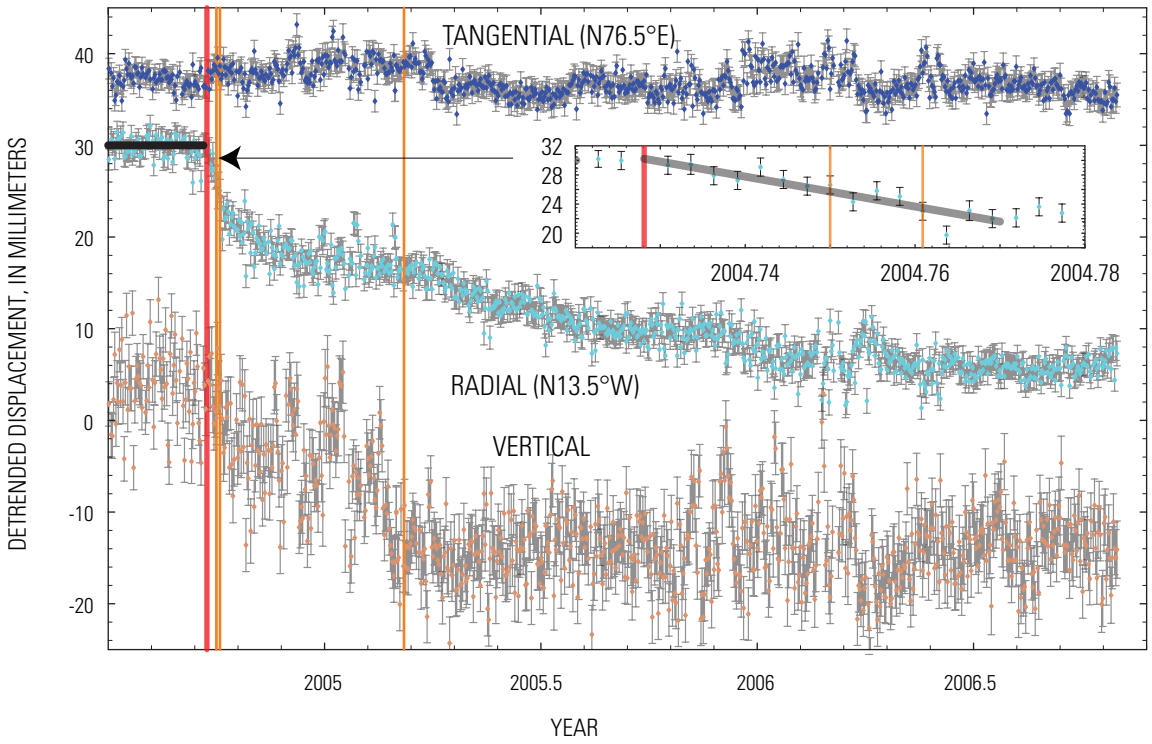

Figure 8. Stacked daily tangential (N. 76.5° E., top), radial (N. 13.5° W., middle), and vertical (bottom) displacements of CGPS station JRO1 from shortly before and during the 2004–2006 dome-building eruption of Mount St. Helens. Error bars are ±1 standard deviation. Bold horizontal black line represents projection of long-term trend in radial displacement, red vertical line marks start of unrest (seismic swarm beginning September 23, 2004), and orange vertical lines show start and end times of a series of phreatic explosions between October 1 and 5, 2004, and the time of last explosion on March 8, 2005. Vertical displacement appears to have ceased shortly after the March 8, 2005, explosion, whereas radial displacement has decayed more slowly. Inset shows a 23-day period at the start of unrest. Winter months show periods of anomalous displacements because of snow and ice accumulation on the GPS antenna radome.

surface, and we would expect associated deformation to be fairly widespread. The propagation of a shallow dike might not produce much deformation at station JRO1, located 9 km from the center of the crater, and we examine data from other stations closer to the newly formed vent for possible offsets at the start of the eruption.

An indirect measure of deformation associated with initial movement of magma to the surface is obtained at the subset of campaign GPS stations that were occupied within a week or two after the start of unrest. Displacement offset of these stations is estimated by projecting the observed 2000 to 2003 position-change trends to the start of unrest (September 23, 2004). We include data from an L1 CGPS station, DOM1, located on the September 1984 lobe of the old dome (see LaHusen and others, this volume, chap. 16). A power failure occurred at DOM1 in January 2004, and the station was not reactivated until September 27, 2004.

The large northward and upward offset at station DOM1 (in the same location as station DMSH) contrasts with the smaller and seemingly random pattern of offsets at surrounding stations (horizontal-displacement offset are shown in fig. 9, and component offsets are listed in table 5). Many of these offsets, though statistically significant on the basis of assumed error estimates, likely result from systematic error in the projected trends. Anomalous 2000 to 2003 velocities (fig. 6) were observed at many of the stations having relatively large event offsets (for example, stations WGOT, BIVO, and SERI, fig.9). These offsets are opposite of the anomalous trends, as might be expected if there were errors in the estimated station velocities. Event deformation appears to be limited to DOM1, which was about 300 m from the newly formed vent. The partially congealed magma plugging the conduit appears to have been pushed to the surface on the south side of the old dome, displacing the old dome slightly to the north and up. Most of the movement at station DOM1 had occurred by the time the station was reactivated (September 27, 2004). In its final days, the station continued moving north until it was destroyed by the first phreatic explosion on October 1, 2004 (LaHusen and others, this volume, chap. 16).

Displacement of GPS Stations During the 2004–2006 Eruption

The inward displacement of CGPS station JRO1 appears to start at about the same time as the first seismic swarm on

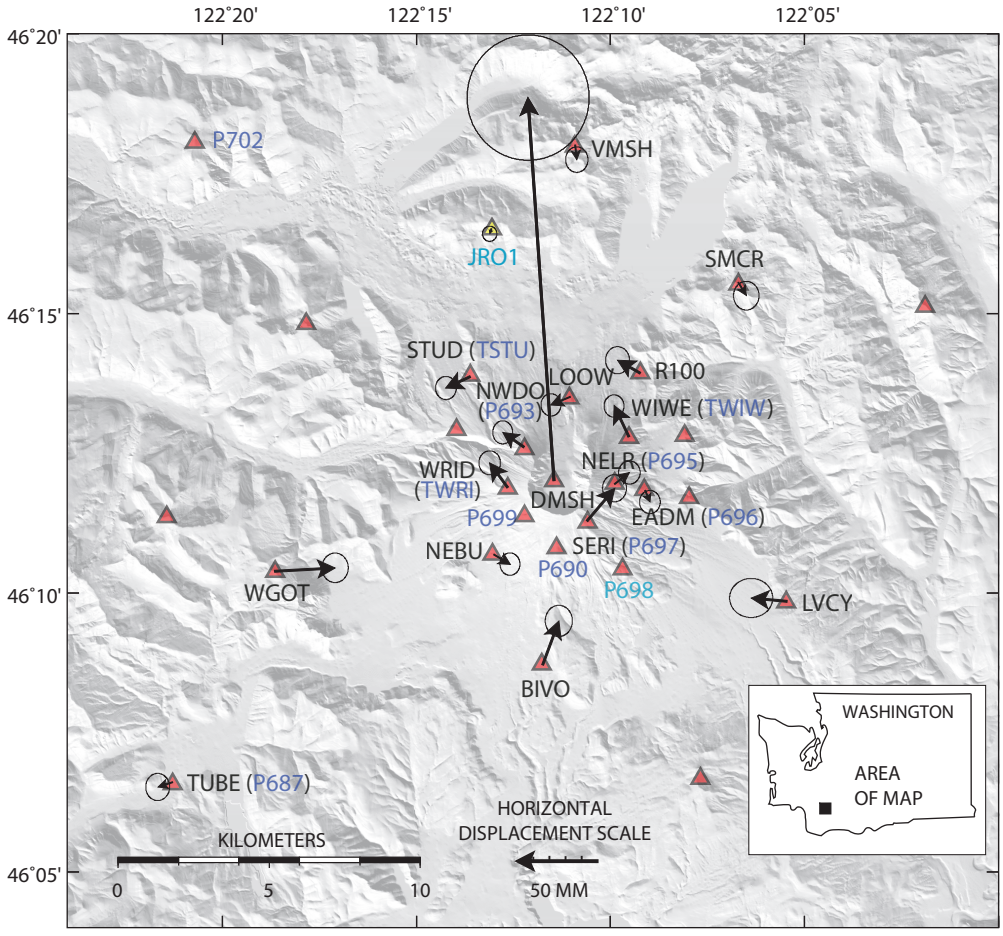

Figure 9. Map showing early event GPS station horizontal-displacement vectors (tipped with 95-percent-confidence error ellipses, vector scale on bottom) in the Mount St. Helens area. Displacements calculated by projecting station velocities to September 23, 2004, and estimating the offset between pre- and post-event positions. Many stations show significant movement, but there is no systematic pattern to suggest intrusion of a new dike to transport magma to the surface. Large displacement on the 1980–86 lava dome is that determined from measurements at DOM1 (same location as DMSH), an L1 CGPS station that was resurrected on September 27, 2004 (LaHusen and other, this volume, chap. 16).

Table 5. Estimated GPS station offsets at start of 2004 seismic unrest.

[Offsets are estimated by projecting 2000–2003 trends to September 23, 2004. Uncertainties are ±1 standard deviation.]

Station	Measurement date (2004)	Longitude (degrees)	Latitude (degrees)	East offset (mm)	North offset (mm)	East-North correlation	Vertical offset (mm)
JRO1	09/28	-122.218	46.275	-1 ± 1.8	-3 ± 1.9	0.004	6 ± 8.7
DOM1	09/28	-122.191	46.200	-16 ± 15.3	235 ± 15.7	0.014	90 ± 40.1
EADM	10/01-10/07	-122.152	46.197	3 ± 2.6	-7 ± 2.9	-0.007	-4 ± 12.2
LOOW	09/28-10/07	-122.184	46.225	-12 ± 2.5	-5 ± 2.8	0.012	-13 ± 11.8
NELR	09/29-10/07	-122.165	46.199	9 ± 2.7	7 ± 2.9	-0.038	3 ± 12.6
NEBU	09/28-10/07	-122.217	46.178	10 ± 2.5	-6 ± 2.8	0.043	-14 ± 12.0
NWDO	09/28-10/07	-122.204	46.210	-13 ± 2.5	9 ± 2.9	-0.002	-3 ± 12.0
SERI	09/30-10/05	-122.177	46.188	17 ± 3.0	20 ± 3.4	-0.070	24 ± 13.7
STUD	09/30-10/07	-122.227	46.231	-15 ± 2.6	-7 ± 2.9	0.016	0 ± 12.1
WIWE	09/29-10/07	-122.159	46.213	-9 ± 2.5	19 ± 2.8	0.021	-7 ± 11.8
WRID	10/01-10/05	-122.211	46.198	-11 ± 2.7	15 ± 3.0	0.024	2 ± 12.9
BIVO	11/03-11/09	-122.196	46.145	10 ± 3.4	27 ± 3.9	0.019	-41 ± 16.1
LVCY	11/04-11/09	-122.091	46.164	-22 ± 5.4	2 ± 4.6	0.057	-3 ± 17.1
R100	11/06 and 11/09	-122.154	46.232	-14 ± 3.0	8 ± 3.4	0.020	-3 ± 14.2
SMCR	11/06 and 11/09	-122.112	46.259	5 ± 3.2	-8 ± 3.6	0.010	-4 ± 14.7
TUBE	11/03-11/07	-122.355	46.110	-9 ± 3.0	-3 ± 3.4	-0.033	-13 ± 13.9
VMSH	11/04-11/09	-122.182	46.300	1 ± 2.8	-9 ± 3.2	0.009	-6 ± 13.3
WGOT	11/04 and 11/05	-122.311	46.173	37 ± 3.3	2 ± 3.7	0.014	-8 ± 15.1

September 23, 2004, and the displacement has continued at a decreasing rate throughout the eruption (fig. 8). The rate of subsidence, however, appears to have leveled off shortly after the March 8, 2005, explosion. Several short periods of anomalous vertical offsets in the winter of 2005, probably the result of snow and ice accumulation on the GPS antenna, make the subsidence appear jerky during the first few months of the eruption. The horizontal components of position change at JRO1 are affected less by winter anomalies, but outliers and short-term variations are apparent in the time series. At the measurement uncertainty of about ±1.7 mm in the horizontal components and ±5 mm in the vertical component of displacement (table 4), there is no apparent deformation anomaly in the months or days before the start of unrest.

The pattern and rate of deformation around Mount St. Helens during all but the first few weeks of the eruption are measured by a network of CGPS stations. Eleven new CGPS stations (seven from PBO and four from CVO) were installed by November 5, 2004 (see table 1 for installation dates and additional information). The PBO stations are part of a planned network of 20 CGPS stations (four with collocated borehole tiltmeters) and four strainmeter stations (each consisting of a borehole tensor strainmeter, a three-component seismometer, and a tiltmeter) in the NSF-funded PBO Mount St. Helens volcanic cluster. The data from new CGPS stations, along with data from JRO1, are processed by CVO as part of the HelensMonit network. Network solutions are transformed into fixed-NOAMgp, ITRF2000, and a local reference frame. The local reference frame for the HelensMonit network consists of five reference stations (GOBS, REDM, KELS, LINH, CVO1).

We use QOCA's time-series analysis to estimate and remove cyclical annual and semiannual seasonal noise from the daily CGPS solutions. We then remove secular tectonic motion predicted by the tectonic model and rotate the resulting cleaned, horizontal-component time series from the east and north geographic components into components that are radial and tangential to Mount St. Helens. At several stations, an eccentric offset correction (table 6) is used to transfer the positions measured at the campaign GPS station early in the eruption to the nearby CGPS station. Then, horizontal and vertical time-series data are stacked to compare position change over time (figs. 10, 11).

The CGPS stations near Mount St. Helens are divided into high- and low-altitude groups for the stacked-component time-series plots. The low-altitude stations have minor winter displacement anomalies, whereas stations at altitudes greater than 2,000 m experience frequent, and sometimes large, winter excursions. The locations of the CGPS stations are shown in figure 9.

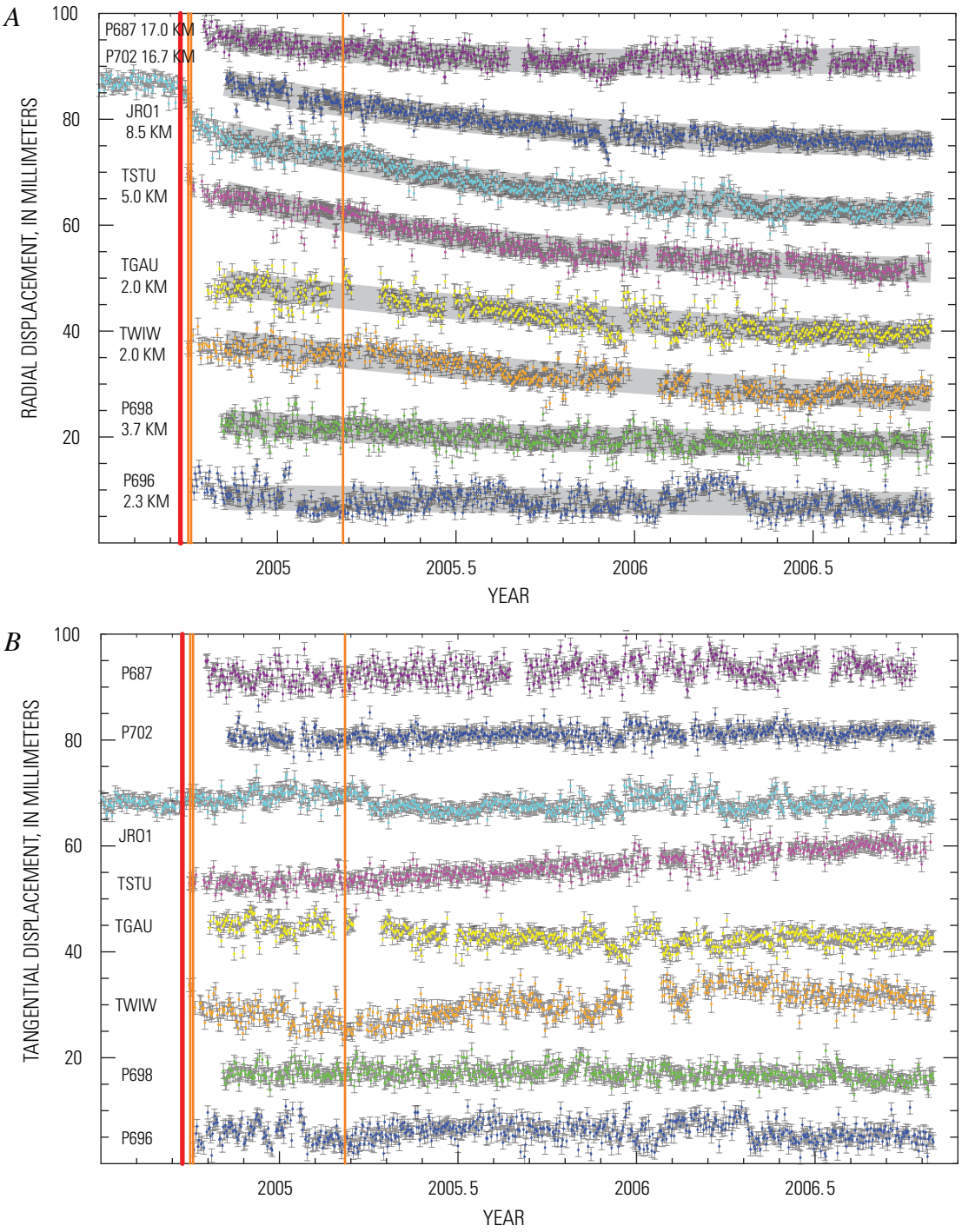

Figure 10. Plots of detrended and stacked time series of daily radial (*A*), tangential (*B*), and vertical (*C*) displacements at eight CGPS stations around Mount St. Helens at altitudes less than 2,000 m. Locations of stations shown in figure 9. Error bars are ±1 standard deviation, and gray bands in radial and vertical displacements are best-fitting rates of exponential decay. The red vertical line marks the start of unrest on September 23, 2004, and the orange vertical lines mark three phreatic explosions. A few of the earliest measurements at TSTU, TWIW, and P696 were made at a nearby campaign GPS station, and an eccentric correction was used to reduce positions to corresponding CGPS station. Tangential displacements at TSTU, TWIW, and TGAU are significantly different than zero. Station distances in *A* and *C* are computed relative to surface projection of modeled source (red cross in fig. 17*A*).

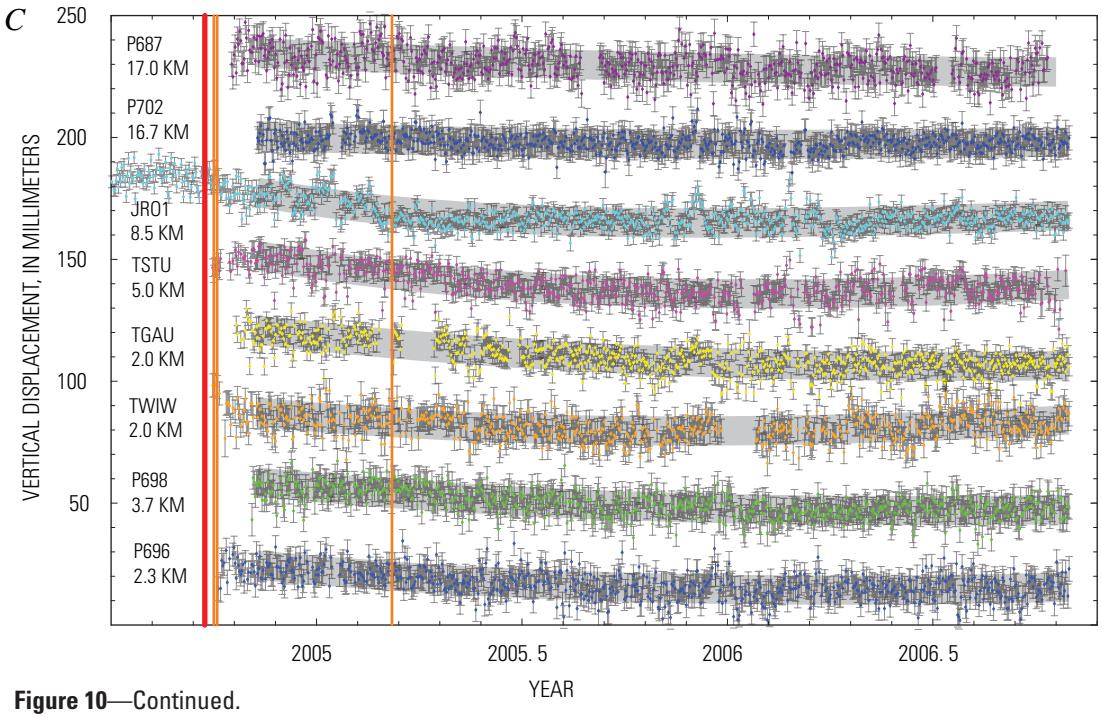

Figure 10—Continued.

The maximum radially inward movement of the low-altitude stations (fig. 10*A*) occurs at stations TSTU and JRO1, located at distances of 5 and 9 km from Mount St. Helens, respectively. Radial movement diminishes at stations located farther (P687, P702) and closer (TGAU, TWIW, P698, P696) to Mount St. Helens. The tangential component of motion is small, except at stations TSTU, TGAU, and TWIW (fig. 10*B*). Subsidence occurs at all stations and reaches its maximum at TSTU, but it diminishes at stations closest to and farthest from Mount St. Helens (fig. 10*C*).

During winter months, CGPS stations installed at altitudes above 2,000 m on Mount St. Helens (P695, P690, TWRI, P693, P697, P699) experience periods of temporary pseudo-displacements (fig. 11) from the accumulation of rime on the GPS antenna (fig. 12). At two high-altitude stations (P690 and P699) where the solar panels were mounted on the south side of the GPS antenna mast, asymmetrical ice loading permanently warped the towers.

The 2004–2005 winter displacements at station P697 were unusually large and constant (fig. 11). Initially we hypothesized that the apparent displacement of this station normal to the south crater wall resulted from the impact of the growing lava spine on that wall. With warming weather in the spring of 2005, the ice covering the GPS antenna melted, and the station returned to its initial position. The winter of 2004–2005 was unusually mild, and large, systematic pseudodisplacements were observed only at the highest stations (P699 and P697), and only the tower for station P699 was warped permanently by ice loading. During the more typical winter of 2005–2006, ice coated the GPS antennas at all high-altitude stations, and the towers at stations P699 and P690 were warped by ice loads on the attached solar panels.

Wintertime pseudodisplacements at the high-altitude CGPS stations complicate analysis of eruption-related deformation there. The application of suitable outlier-rejection criteria in the QOCA time-series analysis minimizes the need for hand-editing data outliers. The calculation of tower offsets at stations P699 (2005 and 2006) and P690 (2006), however, requires careful data editing, and even then the calculated horizontal offsets are poorly determined. The warping of the 3-m-high towers did not appear to cause significant vertical offset. A mechanical offset was introduced at station P699 in September 2006 during site maintenance when a UNAVCO field engineer removed the radome cover and reset the tilted GPS antenna. At the same time, the pole-mounted solar panels at P690 and P699 were removed and replaced with panels mounted on separate frames in an effort to prevent future load-induced offsets.

Time-Decaying Movement of GPS Stations During the 2004–2006 Eruption

The radial and vertical CGPS station displacements have been slowing over time, and the wide, gray bands shown in the stacked radial and vertical displacement plots are best-fitting curves of the form

$$y = ae^{-b(t-t_0)}, \qquad (1)$$

where a and b are constants, t is the observed time, and t_0 is the start time. In the data fit we use October 15, 2004, as the start time and include only data after that date. Our main inter-

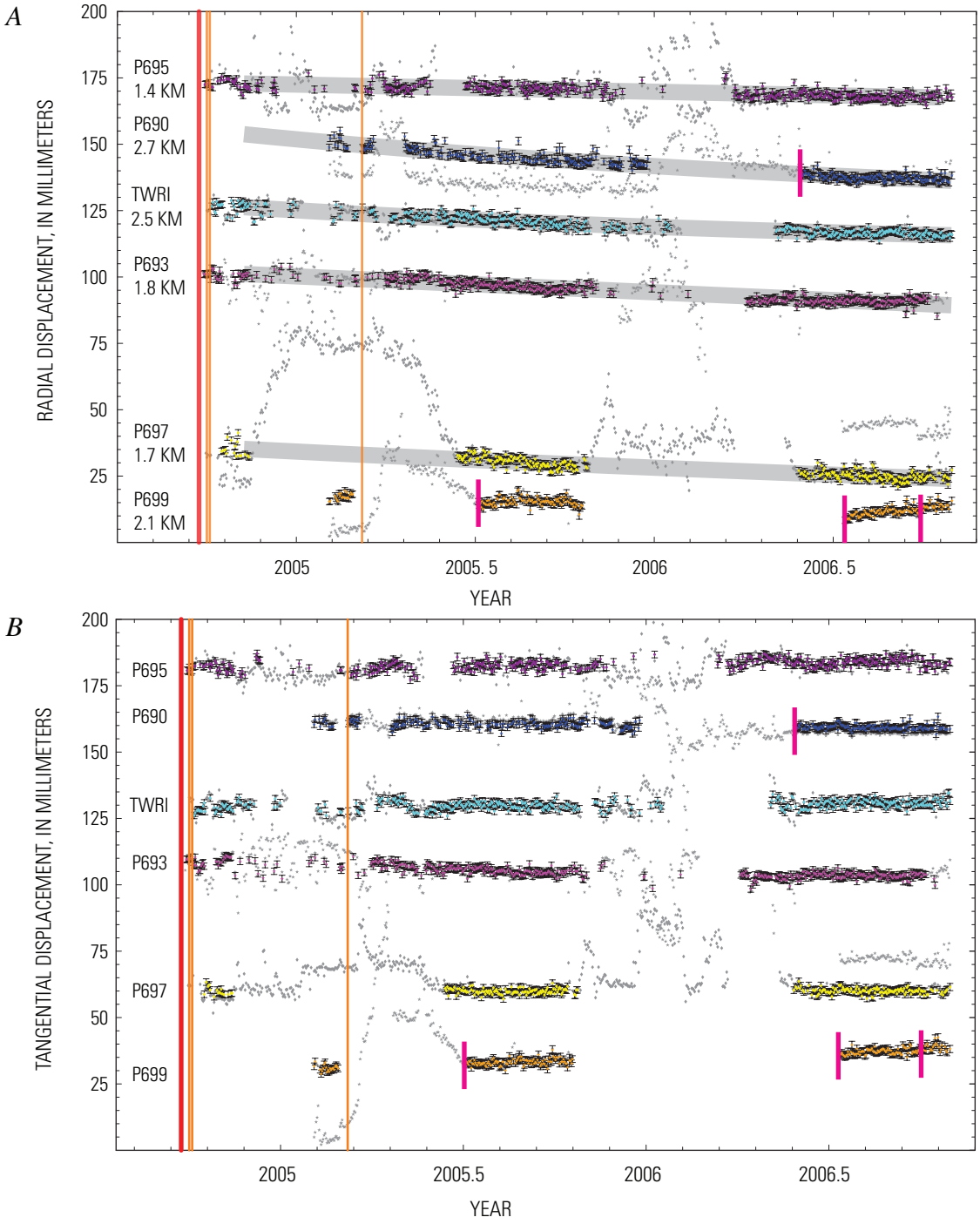

Figure 11. Plots of detrended and stacked time series of daily radial (*A*), tangential (*B*), and vertical (*C*) displacements at six CGPS stations around Mount St. Helens at altitudes greater than 2,000 m. Locations of stations shown in figure 9. Error bars are ±1 standard deviation, and gray bands in radial and vertical displacements are best-fitting rates of exponential decay. Gray dots are outliers (pseudodisplacements) that result from ice coating the GPS antennas, and they are not used in analysis. Short red vertical lines mark time used to calculate an offset for stations P690 and P699 to account for permanent warping of the tower from ice loading. The red vertical line marks the start of unrest on September 23, 2004, and the orange vertical lines mark three phreatic explosions. A few of earliest measurements at P695 and P693 were made at a nearby campaign GPS station, and an eccentric offset correction was used to reduce positions to corresponding CGPS station.

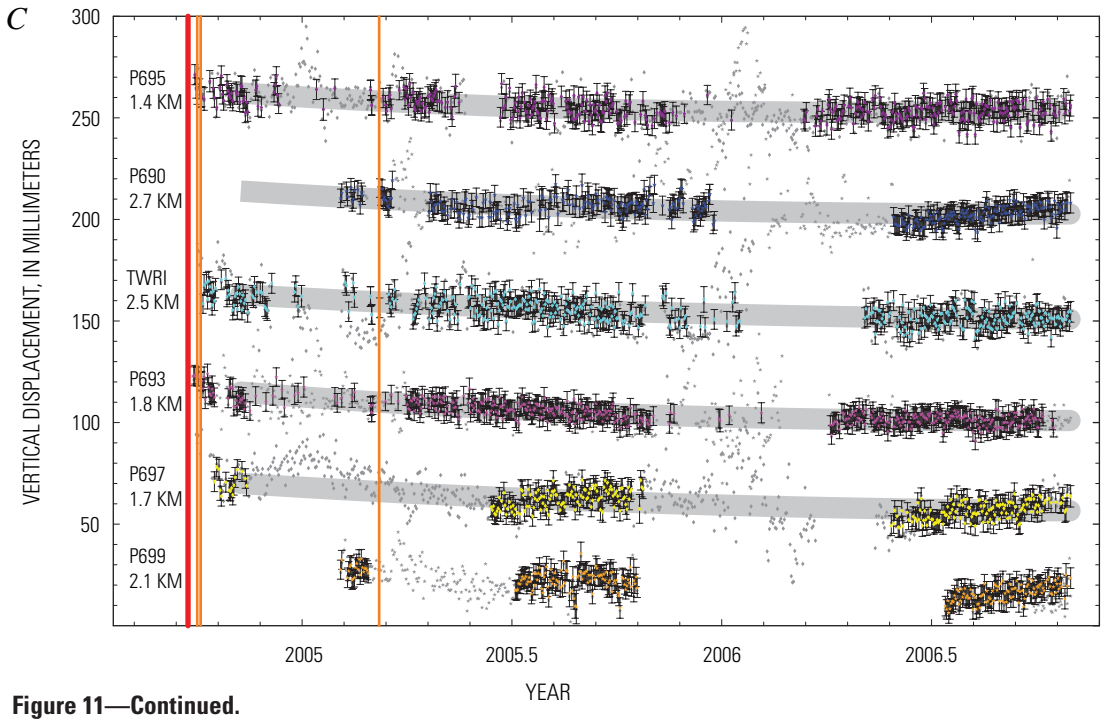

Figure 11—Continued.

Table 6. Surveyed offsets between bedrock campaign GPS stations and nearby tower or braced CGPS stations.

[Offsets may have been surveyed repeatedly and are given in Cartesian coordinates. CGPS, continuously transmitting GPS.]

Bedrock station	CGPS station	Measurement date	X offset (m)	Y offset (m)	Z offset (m)
WIWE	TWIW	2004/10/12	-4.2706	-0.2173	2.2044
WRID	TWRI	2005/08/11-08/18	-71.1883	71.0514	-10.0691
SERI	P697	2005/08/11-08/18	-11.1530	-2.2178	-0.8293
NWDO	P693	2004/10/15-10/19	121.0864	-5.9706	49.7039
STUD	TSTU	2004/10/15	394.1229	211.2114	465.2217
NELR	P695	2004/10/15	36.6088	-37.1623	-30.4480
TUBE	P687	2004/11/03-11/07	1.9623	1.2851	4.3265
SESL	P698	2005/07/13-07/22	50.0780	-53.8675	-15.3364
ELKK	P702	2004/11/05-11/07	-51.9197	-23.0480	-64.4552
EADM	P696	2004/10/15	10.7039	-46.8483	-36.9437
WRAD	P699	2005/08/19	18.1105	-12.8303	19.8468

est is in *b*, which gives the rate of time decay in the displacement components. We add a constant to the residual-component time-series data to make all residual components positive; thus intercept *a* is arbitrary. As discussed previously, the radially inward displacement of JRO1 between September 23 and approximately October 8 averaged 0.5 mm/day (inset, fig. 8). Equation 1 is one of several similar curves derived by Mastin and others (this volume, chap. 22) to fit the volume growth of the dome over time. Changes in the rate of dome growth might be expected to be matched by changes in the rate of volume or mass loss in the magma chamber feeding the eruption. We later test whether the observed deformation can be explained by depressurization of a magma chamber, but first we look for coherent patterns of deformation in the CGPS displacement time series.

Space-Time Correlated Deformation During the 2004–2006 Eruption

The CGPS station-component time series indicate small (total to several centimeters) radially inward and downward movements that appear to have slowed during the eruption. To determine whether these movements are correlated in time, as might be expected if they were in response to pressure loss in a magma reservoir, we apply principal component analysis (PCA; Preisendorfer, 1988). The PCA decomposes the collective station-displacement time series into a number of deformation modes, each of which consists of a common temporal response and a spatial scaling factor that varies between stations but remains constant over time at each station. This method of decomposing space-time data into the superposition of space- and time-separable modes is also called empirical orthogonal-function analysis (Menke, 1984) and eigenanalysis (Aubrey and Emery, 1983). Along with a similar method called Karhunen-Loeve expansion, Dong and others (2006) used PCA to identify and remove common-mode error in daily GPS station-coordinate time series. PCA also has been used to study interseismic deformation (for example, Savage, 1988, 1995).

A mathematical description of the method as applied in QOCA-based PCA analysis is given by Dong and others (2006). Summarizing their discussion, a data matrix X_{ij} is constructed such that each column (subscript i in equation 2) contains a single residual-displacement component (either east, north, or vertical) from a single station in the network. The rows of the matrix (subscript j) include displacement components from all network stations in each period of measurements (daily averages are used here). PCA allows one to represent X_{ij} by

$$X_{ij} = \sum_{k=1}^{N} A_{ik} C_k(t_j), \qquad (2)$$

where the N products $A_{ik}C_k(t_j)$ are the individual modes, with A_{ik} as the spatially varying scale factor and $C_k(t_j)$ as the temporally varying time factor for each mode k. If the PCA-identified deformation modes are ordered by their contribution to the data variance, spatially correlated signals are contained in the first few modes, whereas the higher-order modes usually reflect more local effects.

We apply PCA to the cleaned, residual station-component time series from the 11 Mount St. Helens CGPS stations with the most complete time series (all stations except P690, P697, and P699), three PBO CGPS stations (P420, P421, and P432) located more than 40 km to the north, and the five distant CGPS reference stations (CVO1, KELS, LINH, GOBS, and REDM) included in the solutions. Outliers, predicted tectonic motion, and cyclical annual and semiannual noise are removed from the data. PCA requires observations at all included stations in each epoch. Therefore, Lagrangian interpolation is applied to fill small data gaps, and an iterative process that uses the predictions of the first three PCA modes is used to fill large data gaps (Dong and others, 2006). We examine deformation that occurred after October 15, 2004, when most of the new CGPS stations were operational.

The PCA can identify a single coherent mode of time-varying deformation. The first principal mode (mode 1) accounts for a large percentage (between 40 and 70 percent) of the data variance (fig. 13), particularly in the horizontal components, and only mode 1 temporal components (fig. 14*A*) vary systematically with time. The mode 2 (fig. 14*B*) and higher-order temporal components (not shown) have no long-term changes with time and likely represent random noise and systematic short-term fluctuations at one or more of the analyzed stations.

Mastin and others (this volume, chap. 22) derive logarithmic and exponential functions to fit the time decay in the

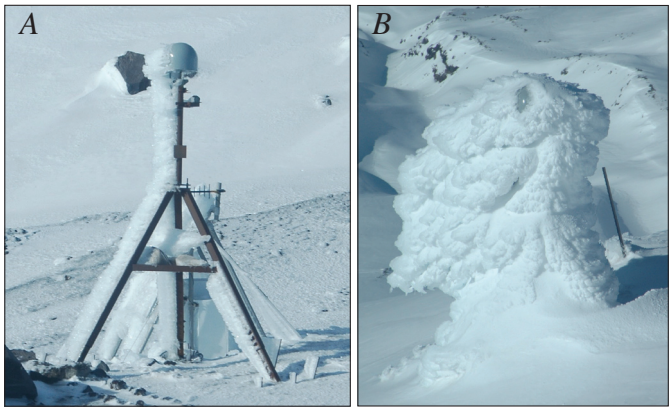

Figure 12. Examples of heavy winter rime on GPS station antennas and tower mounts at altitudes greater than 2,000 m. Locations of stations shown in figure 9. *A*, Station P697. Tower stands 3.5 m above ground, which has been blown free of snow. USGS photo by W.E. Scott. *B*, Station P699. Until September 2006, station P699 had a solar panel mounted on its GPS antenna mast, which exacerbated ice loading and resulted in permanent warping of the tower. USGS photo by M. Lisowski.

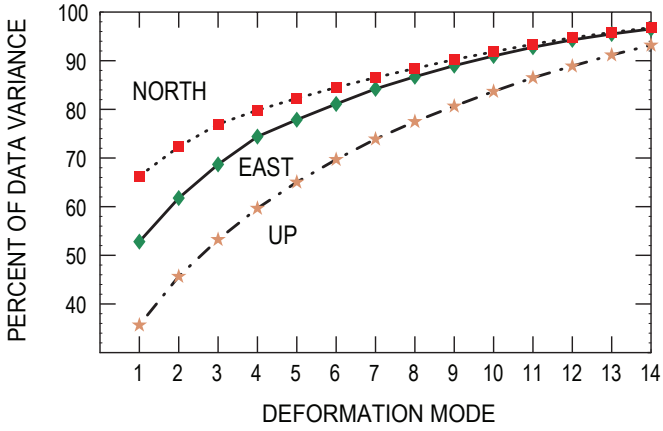

Figure 13. Cumulative percentage of data variance in 14 Mount St. Helens CGPS residual-component time series accounted for by the first 14 PCA deformation modes. North, east, and up spatial components are analyzed independently.

volumetric rate of dome growth and show that a logarithmic decay is expected if flow rate is controlled by frictional sliding of a near-surface plug (provided the coefficient of friction increases with displacement rate), whereas an exponential decay is expected if the effusion rate is a linear function of magma-chamber pressure. Ongoing, constant recharge adds a linear term to the equations of volumetric rate of dome growth.

The mode 1 deformation likely represents the loss of pressure in the magma chamber feeding the eruption, and the mode 1 temporal component can be fit with curves similar to those used by Mastin and others (this volume, chap. 22) to fit dome growth. The mode 1 east and north temporal components are best fit by an exponential decay (equation 1) and by exponential decay with a linear term (table 7). The relatively rapid decrease in the mode 1 vertical component is best fit by

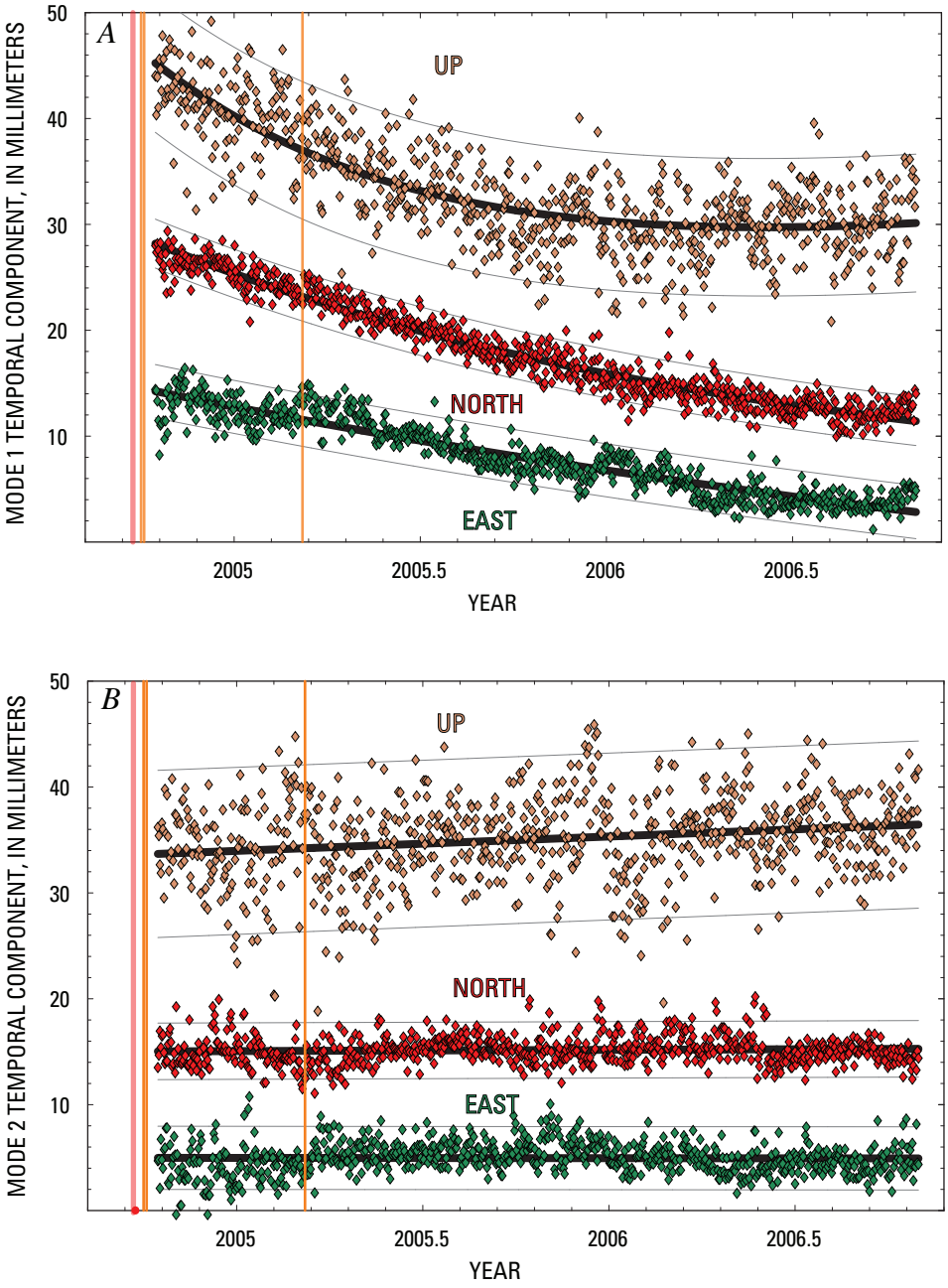

Figure 14. Temporal components from principal component analysis, in millimeters, from the combination of 14 Mount St. Helens CGPS stations and 5 CGPS reference-station residual-component time series. Dark lines are the fits to an exponential decay (equation 1) and light-gray lines are 95-percent-confidence limits of that fit. Vertical orange lines as in figures 10 and 11. *A*, Mode 1. *B*, Mode 2.

an exponential decay with a constant linear increase. The fit of the relatively noisy mode 1 temporal component without a linear term is only slightly worse. In all cases the inverted linear coefficient (*d*) and the exponential time coefficient (*b*) are highly correlated and, therefore, individually poorly determined. The best-fitting curves with the form of equation 1, along with their 95-percent-confidence limits, are shown in figure 14*A*.

So far we have examined only the PCA temporal components $C_k(t_j)$. Scaling the temporal components by the individual station response A_{ik} gives the corresponding station displacement. The scatter in the temporal components, when scaled, will result in scatter in the displacements. To calculate a station displacement for a specified time interval, we need to average or smooth the temporal components. The exponential fit supplies a smoothing that reproduces the data fairly well, and we use it to predict the temporal component and its uncertainty at any given time. The mode 1 horizontal and vertical displacements between October 15, 2004, and October 31, 2006, derived from the exponential fit, are shown in figure 15. Displacements are shown only for close-in stations, so that the map scale remains large enough to display details of deformation near Mount St. Helens, but all displacement values are listed in table 8.

Table 7. Exponential fits to PCA Mode 1 temporal components.

[Constant coefficients for $y=ae^{-b(t-t_0)} + d(t-t_0)$ with $t_0 = 2004.853$.]

Component	a (mm)	b (per yr)	d (mm/yr)	Variance (mm²)
East	22.057	0.366		1.764
East+linear	22.119	0.381	0.163	1.766
North	26.122	0.544		1.432
North+linear	26.077	0.536	-0.075	1.434
Up	24.333	0.471		15.713
Up+linear	29.207	1.171	4.492	13.112

Table 8. PCA Mode 1 station displacements from October 15, 2004, to October 31, 2006.

[Initial and final mode 1 temporal components are scaled by spatial eigenvalue for each station. Estimated 1 standard deviation uncertainty: east, 1.31 mm; north, 1.18 mm; up, 3.59 mm.]

CGPS station	Longitude (degrees)	Latitude (degrees)	East displacement (mm)	North displacement (mm)	Up displacement (mm)
JRO1	237.7824	46.2751	5.0	-14.8	-9.6
TGAU	237.8077	46.2192	4.2	-10.3	-15.3
TSTU	237.7759	46.2369	0.5	-17.2	-14.7
P687	237.6454	46.1096	4.3	-0.4	-8.8
P696	237.8484	46.1969	-0.9	-1.5	-10.3
P698	237.8394	46.1735	-2.7	1.2	-10.2
P702	237.6544	46.3002	6.1	-8.6	-5.5
KELS	237.1039	46.1182	3.7	-2.6	0.8
P693	237.7977	46.2103	8.1	-6.4	-9.3
P695	237.8358	46.1990	-3.2	-1.3	-9.2
TWIW	237.8413	46.2129	-11.5	-3.2	-9.3
P420	237.1337	46.5886	1.4	-3.9	-0.1
P421	237.5708	46.5319	2.4	-5.7	-5.0
P432	238.3168	46.6229	0.1	-3.7	-3.3
GOBS	239.1853	45.8388	-0.7	1.3	-0.8
LINH	239.4615	47.0003	0.3	-1.1	0.7
CVO1	237.5039	45.6109	0.1	-1.5	-1.4
REDM	238.8521	44.2598	0.3	-0.1	-0.7
TWRI	237.7881	46.1979	7.8	-4.5	-9.7

A few general features are apparent in the mode 1 displacements shown in figure 15. Maximum horizontal and vertical displacements are roughly equal, and subsidence is observed everywhere, with maximum values at distances greater than about 3 km and less than about 10 km. Horizontal displacements are toward Mount St. Helens, with maximum values at distances greater than about 5 km and less than about 20 km, and they are larger to the north of Mount St. Helens than to the south. Some of the apparent asymmetry in the deformation could result from the fact that there are more CGPS stations north of Mount St. Helens. Some other possible explanations for the asymmetry include error in the tectonic model that underestimates the background rate of northward motion, a source of deformation that is located to the south of the crater, a dipping source, and a laterally inhomogeneous crust.

The CGPS station displacements can be supplemented with data from a few campaign GPS stations to increase the areal coverage. This combination will be used to constrain possible sources of deformation. When we have a suitable model, we use the PCA mode 1 deformation to estimate the change in time.

Analytical Source Models

By using the PCA, a single mode of time-varying deformation was identified in the cleaned CGPS time series, which consists of an exponentially decaying downward and inward collapse toward Mount St. Helens. Such a collapse can result from pressure loss in the magma chamber feeding the eruption.

A simple model of an erupting volcano includes a magma chamber and a conduit to allow magma to escape to the surface (fig. 16). Magma chambers are idealized as fluid-pressurized, ellipsoidal cavities in an elastic half-space (Mogi, 1958; Davis and others, 1974; Davis, 1986; Yang and others, 1988; Fialko and others, 2001), and conduits are idealized as verti-

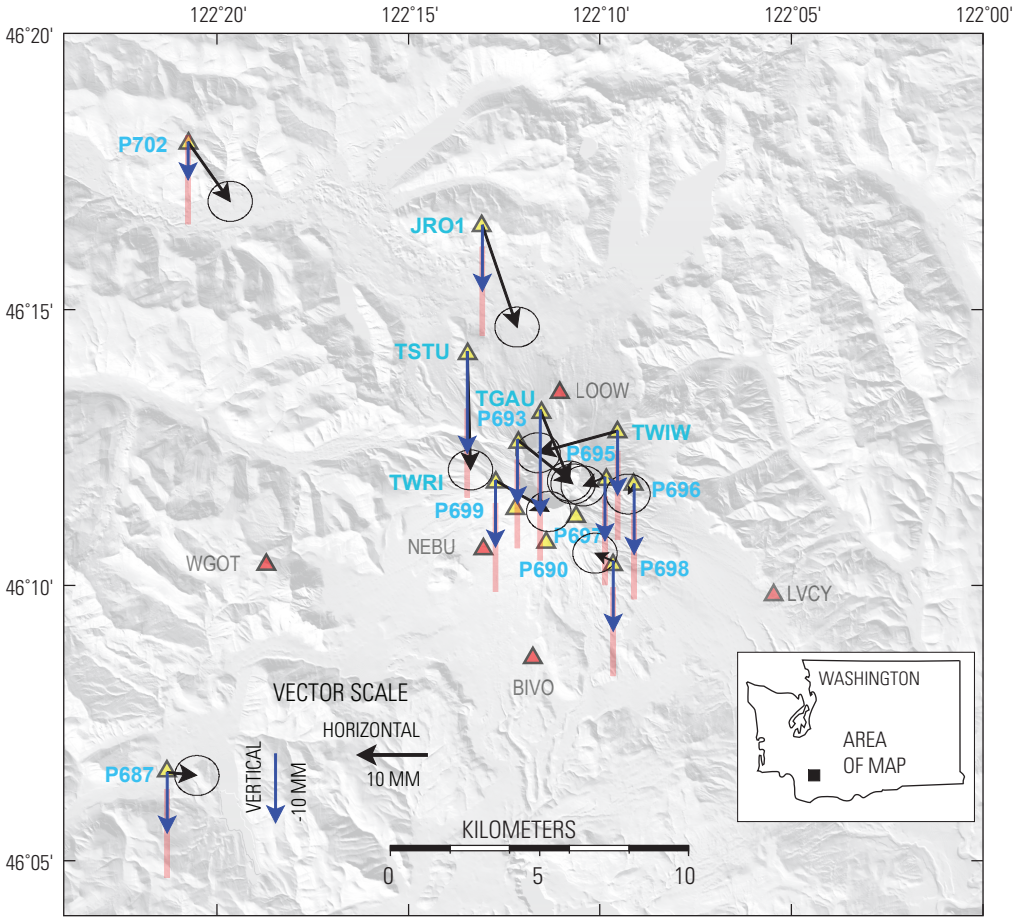

Figure 15. Map showing PCA mode 1 estimated horizontal (black arrows, tipped with 95-percent-confidence error ellipses) and vertical (blue arrows tipped with orange 95-percent-confidence error bars) displacements from October 15, 2004, to October 31, 2006, for the Mount St. Helens area. CGPS stations P699, P690, and P697 are not included in PCA analysis because of offsets and persistent winter excursions.

cal closed or open pipes (Bonaccorso and Davis, 1999). The eruption will continue until overpressure in the magma system drops below that of an equilibrated open magmatic system or until the conduit is blocked by congealing magma. As magma is withdrawn to feed an eruption, the pressure decrease in the magma system can be buffered by exsolution of gas (Mastin and others, this volume, chap. 22) and by input of new magma from depth.

Pressure change in a conduit with a radius of 10–50 m, typical for volcanoes (Bonaccorso and Davis, 1999), contributes little to the surface deformation, except near the vent; for the same reason, we can ignore deformation produced by shear tractions on the wall of the conduit exerted by magma flowing through the conduit. We assume that pressure change in the magma reservoir beneath the conduit is responsible for most of the observed deformation; therefore, we use the data to constrain the approximate limits of source depth, geometry, and the cavity volume change of a pressure source that represents the magma chamber. We limit our search to spheroidal pressure sources, which include spheres and prolate (elongate) and oblate (flattened) spheroids. We assume Poisson's ratio equals 0.25, and that the shear modulus equals 30 GPa in all the models. The pressure change that best reproduces the deformation is not estimated directly; rather, it is combined with the elastic parameters (shear modulus G, and Poisson's ratio ν) and the unknown source volume. Paradoxically, except for very shallow sources (where the chamber size is a large fraction of the depth), a large pressure change in a small source volume is indistinguishable from a small pressure change in a large source volume (McTigue, 1987). The ratio of pressure change to shear modulus must remain within the elastic limits of the surrounding rock.

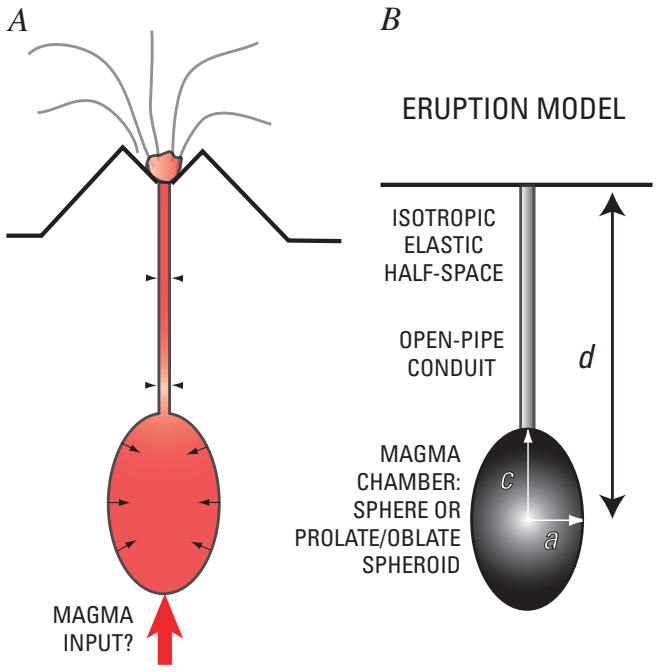

Figure 16. Schematic cross section of erupting volcano (*A*) and pressure sources (*B*) used to model surface deformation. Source depth, d, of magma chamber in half-space is relative to mean elevation of volcano.

Combined CGPS and Campaign GPS Data

Stations in the CGPS network are concentrated around the crater and to the north of Mount St. Helens. To improve spatial coverage of the deformation, we add data from campaign GPS surveys at five stations located at moderate distances from Mount St. Helens (red triangles in fig. 17). These stations were surveyed, at minimum, in late 2004 and again in 2005. We assume that deformation accumulates at a constant rate during the year after October 11, 2004, and obtain average station velocities for CGPS and campaign GPS stations (table 9). Our start and stop dates are arbitrary, but they include surveys of all the key campaign GPS stations. The mode 1 temporal components (fig. 14*A*) decay at approximately a linear rate during this year-long interval, except for the relatively noisy vertical component. The average horizontal (fig. 17) and vertical (fig. 18) station velocities for this one-year period are comparable in direction and relative magnitude to those derived from the PCA for a two-year period. Note that we include velocities for stations P690 and P697, which were excluded from the PCA analysis because of winter anomalies. The uncertainties in the station velocities are those from the QOCA time-series analysis supplemented in quadrature with a random-walk error of 1 mm/yr.

Elastic Half-Space Deformation Source Models

The nearly radial symmetry in the eruption-related deformation is consistent with a spheroidal-source geometry, and we first fit the data to a spherical-point (also called Mogi) pressure source by using a random-cost (Berg, 1993; Murray and others, 1996) search algorithm for the optimal location and depth of the source. Use of a point-source model is justified because the deformation is widespread, and, therefore, consistent with a source that is much deeper than its size (McTigue, 1987). The best-fitting spherical point-source depth (table 10) is deep (13 km), but, as indicated by the data misfit (reduced χ^2) of greater than 2, it is a poor choice when the maximum vertical and horizontal deformation are roughly equal (fig. 19*A*). A spherical source predicts a maximum horizontal deformation that is about 0.4 of the maximum vertical. Some of the misfit of the data to the model may be from the tectonic model used to correct the observed velocities. To account for such systematic error, we solve for a constant horizontal velocity in the data inversion. The point source with a systematic velocity shift fits the data slightly better, having a shallower source depth, and the center of deformation is shifted slightly to the northwest. The components of the translation (1.4 mm/yr west, 2.1 mm/yr north), however, are considerably larger than the misfit of the tectonic model to the pre-event velocity of JRO1 (0.5 mm/yr west, 0.9 mm/yr north).

A prolate spheroidal (cigar-shaped) pressure source predicts roughly equal maximum horizontal and vertical

Table 9. Adjusted Helens CGPS average station velocities from October 11, 2004, to October 11, 2005.

[Velocities are in nominal ITRF2000 fixed North American Plate terrestrial reference frame and are corrected for regional rigid-body rotation and strain.]

Station	Longitude (degrees)	Latitude (degrees)	East velocity ± 1 σ error (mm/yr)	North velocity ± 1 σ error (mm/yr)	Up velocity ± 1σ error (mm/yr)
JRO1	-122.2180	46.2750	5.42 ± 1.09	-10.50 ± 1.10	-13.19 ± 1.45
TSTU	-122.2240	46.2370	2.92 ± 1.09	-11.02 ± 1.10	-15.48 ± 1.46
TGAU	-122.1920	46.2190	3.78 ± 1.10	-5.32 ± 1.11	-12.58 ± 1.51
TWIW	-122.1590	46.2130	-5.53 ± 1.10	-2.24 ± 1.11	-8.49 ± 1.50
TWRI	-122.2120	46.1980	7.03 ± 1.13	-2.46 ± 1.14	-9.21 ± 1.64
P687	-122.3550	46.1100	4.56 ± 1.10	1.69 ± 1.11	-5.75 ± 1.54
P690	-122.1900	46.1800	0.56 ± 1.43	7.88 ± 1.48	-7.63 ± 2.71
P693	-122.2020	46.2100	7.41 ± 1.14	-2.59 ± 1.16	-8.98 ± 1.67
P695	-122.1640	46.1990	-2.08 ± 1.13	0.50 ± 1.14	-8.41 ± 1.66
P696	-122.1520	46.1970	-1.13 ± 1.10	0.32 ± 1.11	-9.11 ± 1.51
P697	-122.1770	46.1880	1.44 ± 1.33	0.58 ± 1.37	-3.30 ± 2.45
P698	-122.1610	46.1730	-1.72 ± 1.11	2.33 ± 1.12	-10.52 ± 1.56
P702	-122.3460	46.3000	5.44 ± 1.12	-7.10 ± 1.13	-3.45 ± 1.57
NEBU	-122.2170	46.1780	5.15 ± 1.77	0.65 ± 1.85	-14.71 ± 3.80
BIVO	-122.1960	46.1450	-1.43 ± 1.19	7.55 ± 1.21	-5.01 ± 1.88
LVCY	-122.0910	46.1640	-5.56 ± 2.16	3.25 ± 2.23	-11.54 ± 4.69
LOOW	-122.1840	46.2250	-0.35 ± 1.84	-7.65 ± 1.91	-10.02 ± 3.91
WGOT	-122.3110	46.1730	5.20 ± 2.40	1.90 ± 2.49	-15.80 ± 5.07
P420	-122.8660	46.5890	1.40 ± 1.08	-1.85 ± 1.09	0.94 ± 1.43
P421	-122.4290	46.5320	2.02 ± 1.17	-3.78 ± 1.19	-1.44 ± 1.79
P432	-121.6830	46.6230	-0.65 ± 1.09	-1.94 ± 1.10	-2.39 ± 1.44
KELS	-122.8960	46.1180	2.07 ± 1.08	-0.81 ± 1.09	-0.23 ± 1.38
GOBS	-120.8150	45.8390	0.86 ± 1.08	-1.55 ± 1.09	-1.10 ± 1.38
CVO1	-122.4960	45.6110	1.41 ± 1.08	0.04 ± 1.09	-0.65 ± 1.38
REDM	-121.1480	44.2600	-0.51 ± 1.08	-0.68 ± 1.09	0.65 ± 1.38
LINH	-120.5390	47.0000	-1.50 ± 1.08	-0.43 ± 1.09	2.26 ± 1.39

deformation. A point source of this type can be constructed by superimposing three collocated orthogonal point cracks (for example, Okada, 1985, 1992), with two of the cracks having equal amplitudes related to the aspect ratio w of the minor radii to the major radius of the spheroid by

$$M_0 = 1/(0.3 - 0.1w), \quad (3)$$

and the third crack having an amplitude

$$M_0 = 1/(0.4w - 0.2). \quad (4)$$

M_0 is the moment, which in this case is equivalent to volume change (the amount of opening times the area affected) multiplied by the shear modulus. If we substitute $w = 1$, then $M_0 = 5$ for the sum of all three cracks, and the source obtained is equivalent to a spherical point pressure source. Decreasing w elongates the spheroid.

A point prolate spheroidal pressure source with its long axis vertical fits the data better than do the spherical point-source models (table 10, fig. 19*B*). The best-fitting aspect ratio (0.66) and depth (7.9 km) is roughly consistent with other models of the Mount St. Helens magma chamber (Pallister and others, 1992). Only a slight improvement in the fit is obtained by adding a systematic horizontal velocity (0.2 mm/yr west, 1.4 mm/yr north), which shifts the center of the source to the southwest. The estimated velocity shift is similar to the misfit of the tectonic model to the pre-event velocity of JRO1.

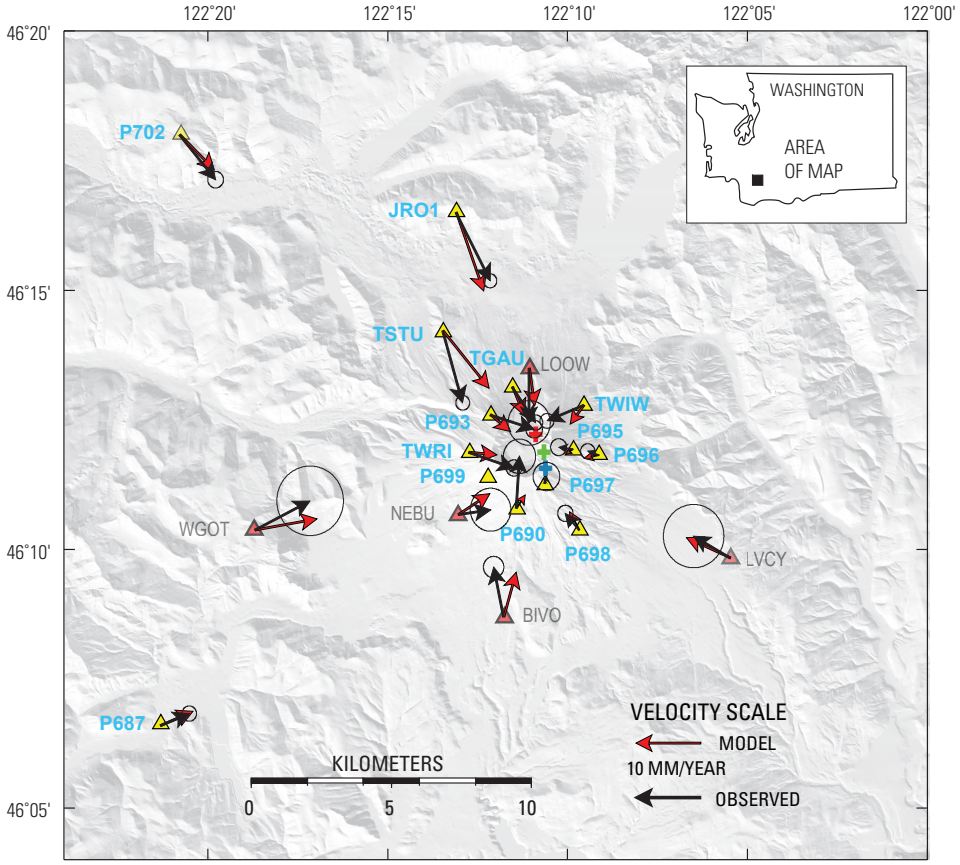

Figure 17. Map showing corrected average GPS station horizontal-velocity vectors (black arrows tipped with 95-percent-confidence error ellipses) and displacements predicted by best-fitting, tilted point prolate spheroid (red arrows, scale at bottom of figure) for the Mount St. Helens area from October 15, 2004, to October 15, 2005. See table 10 for model parameters. Surface projection of center of tilted point prolate spheroid marked by red cross, that of vertical prolate spheroid by blue cross, and that of spherical point pressure source by green cross.

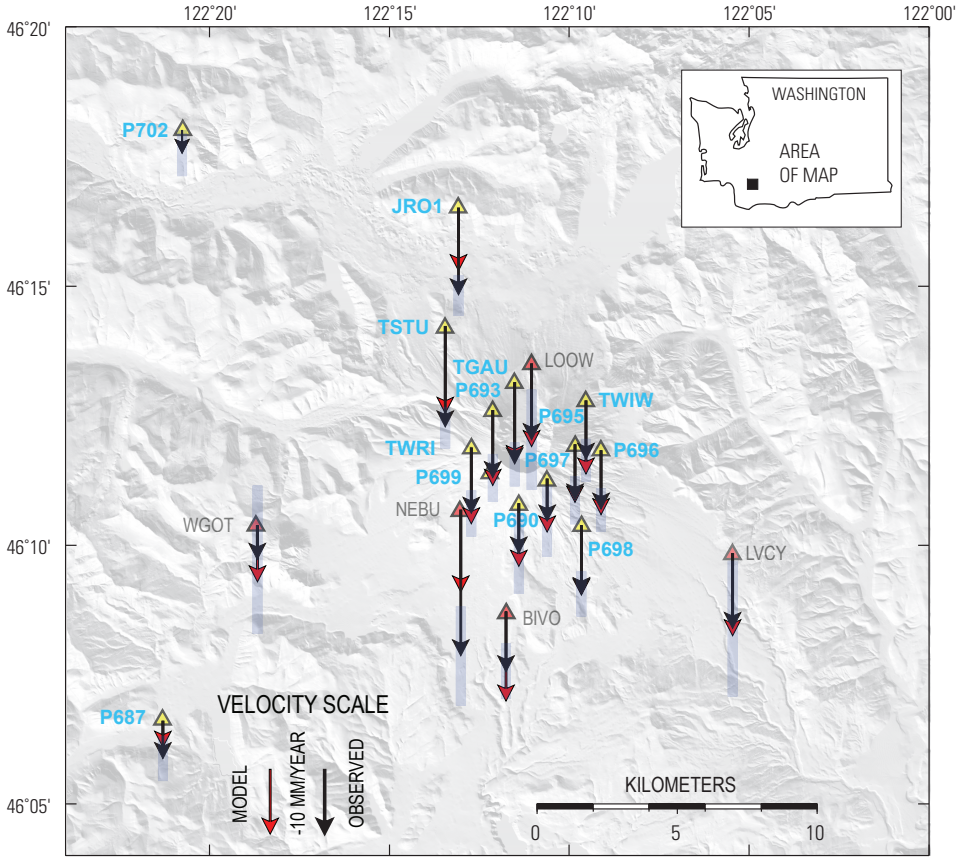

Figure 18. Map showing corrected average GPS station vertical-velocity vectors (black arrows tipped with light blue 95-percent-confidence error bar) and vertical displacements predicted by best-fitting, near-vertical, point-prolate spheroid (red arrows, scale at bottom) for Mount St. Helens area from October 15, 2004, to October 15, 2005. See table 10 for model parameters.

Another way for the model to account for asymmetry in the deformation is to allow the source to plunge at an angle less than 90º and to allow the azimuth of this axis to vary. If we do not allow for a systematic rate of translation, the parameter search returns a vertical optimal plunge. If we allow for a systematic velocity error, the best-fitting, plunging prolate source is nearly vertical (83º) with azimuth N. 37º W. (fig. 19*C*). The systematic velocity is again similar to the misfit of the tectonic model to the pre-event velocity of JRO1.

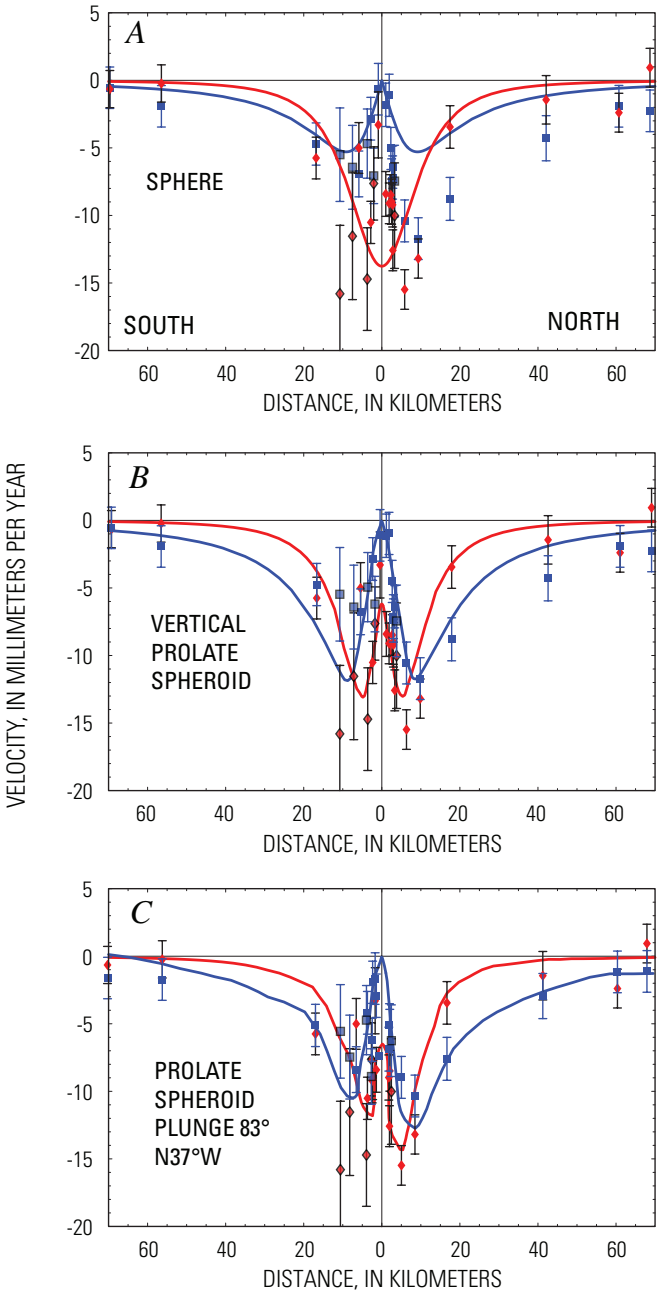

Figure 19. Observed radial (blue squares) and vertical (red diamonds) velocities for deformation of Mount St. Helens from October 15, 2004, to October 15, 2005, projected onto north-south profile and compared with predicted radial (solid blue curve) and vertical (red curve) velocities from best-fitting point sources. Error bars are ±1 standard deviation. Details of models given in table 9. *A*, spherical point pressure source; *B*, vertical point prolate spheroid; *C*, tilted or dipping point prolate spheroid with a small velocity correction.

To calculate the volume change consistent with the source strength, we assume that the spherical source has a radius of 1 km and the prolate spheroid has a minor radius of 1 km. Once the model geometry is fixed to the values obtained by the parameter search, the radius change (equivalent to strength of the source) is inverted directly. The equivalent source cavity-volume decrease for the one-year period covered by the data is in the range 8–12×10^6 m^3 in the various prolate spheroid models.

Only JRO1 recorded the relatively rapid deformation that occurred during the first two weeks of the eruption, and we use its motion as a proxy to estimate the total cavity-volume loss. The predicted 12.8 mm/yr of radially inward motion at JRO1 from the dipping prolate spheroid model with a systematic velocity correction is about half of the total movement of JRO1 from September 23, 2004, to October 31, 2006. A total cavity-volume loss of 16–24×10^6 m^3 is consistent with the JRO1 displacements, and it is a fraction of the >83×10^6 m^3 dome volume as of August 2006. Mastin and others (this volume, chap. 22) explain this discrepancy as a combination of exsolution of gas, which buffers pressure loss in the magma chamber, and recharge by new magma (recharge estimated to be only about one-tenth of the erupted volume). The recharge, if it is occurring, has thus far not increased the flux of volcanic gases (Gerlach and others, this volume, chap. 26).

Conclusions

Remarkably little far-field volcanic deformation has occurred around Mount St. Helens since shortly after the crater-forming collapse and eruption in 1980. Data collected in 1982 and 1991 for surveys of a regional high-precision trilateration network provide the clearest evidence for recharge of the volcano's magma system. During that interval, areal dilatation accumulated at an average rate of 144±39 nanostrain/yr, an order of magnitude greater than and opposite in sign to the estimated background rate of −15±3 nanostrain/yr. No significant deformation occurred in the same network between 1991 and 2000.

GPS surveys conducted since the 1990s reveal background deformation, which is used to define a tectonic model that includes a rigid-body clockwise rotation and a small amount of strain accumulation. The background strain accumulation within the network (in the absence of volcano deformation) is essentially a uniaxal contraction in the east-northeast direction, a possible effect of a locked Cascadia subduction-zone thrust fault. After removing this secular deformation, we find no coherent pattern of volcanic deformation around Mount St. Helens between 2000 and 2003. Furthermore, daily position measurements made at a CGPS

Table 10. Elastic half-space deformation source models.

[ΔEast and ΔNorth data show estimates for rigid-body translation rate that account for possible error in tectonic model. --, elements not part of solution; n.a., not applicable to long-axis trend because model is of vertical prolate geometry.]

Source description	Longitude (degrees)	Latitude (degrees)	Depth (km)	ΔRadius (m/yr)	ΔEast (m/yr)	ΔNorth (m/yr)	Aspect ratio	Long axis plunge (degrees)	Long axis (trend)	Model parameters	Reduced χ^2	ΔVolume (10^6 m^3/yr)
Spherical point pressure (Mogi)	-122.1765	46.1961	12.93	-0.7653	--	--	1.00 (fixed)	--	--	4	2.17	9.7
Spherical point pressure + translation rate	-122.1926	46.2119	10.39	-0.5028	-0.0014	0.0021	1.00 (fixed)	--	--	6	1.95	6.3
Vertical prolate spheroid	-122.1746	46.2133	7.99	-1.1485	--	--	0.66	90 (fixed)	n.a.	5	1.59	11.9
Vertical prolate spheroid + translation rate	-122.1758	46.2000	7.60	-0.9651	-0.0002	0.0014	0.673	--	n.a.	7	1.54	9.6
Tilted prolate spheroid	-122.1748	46.2133	7.94	-1.1356	--	--	0.660	90 (fixed)	n.a.	7	1.60	11.9
Tilted prolate spheroid + translation rate	-122.1811	46.2133	7.14	-0.7927	-0.0004	0.0013	0.676	82.4	N36°W	9	1.49	7.9

station 9 km north of Mount St. Helens show no anomalous deformation from 1997 until the start of seismic unrest on September 23, 2004.

The movement of magma to the surface at the start of unrest did not systematically displace GPS stations on the volcano's flanks, but it did displace station DOM1 on the September 1984 lobe of the old dome by more than 0.2 m to the north. The lack of systematic deformation around the crater suggests that solidified magma plugging the top of the conduit was pushed out, rather than being bypassed. Much of the movement of the L1 CGPS station DOM1 occurred by September 28, well before the first phreatic explosion, suggesting that the movement of magma began with the start of seismic unrest. At the same time, CGPS station JRO1 moved toward Mount St. Helens an average of about 0.5 mm/day from September 23 until a few days after the phreatic explosion on October 5, 2004, when its motion slowed and began to decay.

Analysis of eruption-related deformation data reveals a single space- and time-coherent mode of time-varying deformation, which has been decaying exponentially since the start of unrest. All GPS stations are moving toward Mount St. Helens and downward in a manner consistent with the predictions of an elastic half-space model that represents pressure loss in a vertically elongate magma chamber. The center of Mount St. Helens' magma chamber is estimated to be at a depth of 7 to 8 km, and the chamber's long axis, which is vertical or near vertical, is estimated to be approximately three times longer than its diameter. The actual dimensions of the magma chamber are poorly constrained by the deformation data. The source-cavity volume loss, which is proportional to the strength of the source, is about $16–24\times10^6$ m^3, about one-third of the erupted volume. This discrepancy can be accounted for mostly by buffering of pressure loss in the magma chamber through exsolution of gas and with a small amount of recharge (Mastin and others, this volume, chap. 22).

Acknowledgments

We thank the NSF-sponsored Plate Boundary Observatory for rapid installation of CGPS monitoring stations in October 2004 in response to renewed unrest at Mount St. Helens. In particular, we are grateful for the timely efforts of Katrin Hafner and other field engineers from UNAVCO, Inc., the contractor responsible for installing PBO stations.

We thank the CVO staff, temporary staff, and volunteers who helped with the field surveys and permanent CGPS station construction. We are grateful that Elliot Endo had the foresight to install a CGPS station at the Johnston Ridge Observatory. Richard LaHusen established telecommunications at the U.S. Forest Service's Coldwater Ridge maintenance shed in order to download CVO GPS data, and he provided L1 CGPS data. We used computer code from John Langbein of the USGS Earthquake Hazards Team to invert for best-fitting source-model parameters. The original code was developed by James C. Savage; Mark H. Murray added random-cost extensions and the Okada dislocation routines, and John Langbein added code for the ellipsoidal pressure sources. John Langbein and Larry Mastin provided constructive reviews of this paper.

References Cited

Aubrey, D.G., and Emery, K.O., 1983, Eigenanalysis of recent United States sea levels: Continental Shelf Research, v. 2, p. 21–33.

Altimimi, Z., Sillard, P., and Boucher, C., 2002, ITRF2000: A new release of the International Terrestrial Reference Frame for earth science applications: Journal of Geophysical Research, v. 107, no. B10, 2214, doi:10.1029/2001JB000561.

Berg, B., 1993, Locating global minima in optimization problems by a random-cost approach: Nature, v. 361, p. 708–710.

Blewitt, G., 1989, Carrier phase ambiguity resolution for the Global Positioning System applied to geodetic baselines up to 2000 km: Journal of Geophysical Research, v. 94, no. B8, p. 10187–10203.

Bonaccorso, A., and Davis, P.M., 1999, Models of ground deformation from vertical volcanic conduits with application to eruptions of Mount St. Helens and Mount Etna: Journal of Geophysical Research, v. 104, no. B5, p. 10531–10542.

Davis, P.M., 1986, Surface deformation due to inflation of an arbitrarily oriented triaxial ellipsoidal cavity in an elastic half-space, with reference to Kilauea volcano: Journal of Geophysical Research, v. 91, p. 7429–7438.

Davis, P.M., Hastie, L.M., and Stacey, F.D., 1974, Stresses within an active volcano, with particular reference to Kilauea: Tectonophysics, v. 22, p. 363–7438.

Demets, C., Gordon, R.G., Argus, D.F., and Stein, S., 1994, Effect of recent revisions of the geomagnetic reversal timescale on estimates of current plate motions: Geophysical Research Letters, v. 21, p. 2191–2194.

Dong, D., Herring, T.A., and King, R.W., 1998, Estimating regional deformation from a combination of space and terrestrial geodetic data: Journal of Geodesy, v. 72, p. 200–214.

Dong, D., Fang, P., Bock, Y., Cheng, M.K., and Miyazaki, S., 2002, Anatomy of apparent seasonal variations from GPS-derived site position time series: Journal of Geophysical Research, v. 107, no. B4, p. ETG 9-1–ETG 9-16.

Dong, D., Fang, P., Bock, Y., Webb, F., Prawirodirdjo, L., Kedar, S., and Jamason, P., 2006, Spatiotemporal filtering using principal component analysis and Karhunen-Loeve expansion approaches for regional GPS network analysis: Journal of Geophysical Research, v. 111, no. B03405, doi:10.1029/2005JB003806.

Dvorak, J., Okamura, A., Mortensen, C., and Johnston, M.J.S., 1981, Summary of electronic tilt studies at Mount St. Helens, *in* Lipman, P.W., and Mullineaux, D.R., eds., The 1980 eruptions of Mount St. Helens, Washington: U.S. Geological Survey Professional Paper 1250, p. 169–174.

Ewert, J.W., and Swanson, D.A., 1992, Monitoring volcanoes; techniques and strategies used by the staff of the Cascades Volcano Observatory, 1980–90: U.S. Geological Survey Bulletin 1966, 223 p.

Fialko, Y., Khazan, Y., and Simons, M., 2001, Deformation due to a pressurized horizontal circular crack in an elastic half-space, with applications to volcano geodesy: Geophysical Journal International, v. 146, p. 181–190.

Gerlach, T.M., McGee, K.A., and Doukas, M.P., 2008, Emission rates of CO_2, SO_2, and H_2S, scrubbing, and preeruption excess volatiles at Mount St. Helens, 2004–2005, chap. 26 *of* Sherrod, D.R., Scott, W.E., and Stauffer, P.H., eds., A volcano rekindled; the renewed eruption of Mount St. Helens, 2004–2006: U.S. Geological Survey Professional Paper 1750 (this volume).

Heflin, M., Bertiger, W., Blewitt, G., Freedman, A., Hurst, K., Licten, S., Lindqwister, U., Vigue, Y., Webb, F., Yunck, T., and Zumberge, J., 1992, Global geodesy using GPS without fiducial sites: Geophysical Research Letters, v. 19, no. 2, p. 131–134.

LaHusen, R.G., Swinford, K.J., Logan, M., and Lisowski, M., 2008, Instrumentation in remote and dangerous settings; examples using data from GPS "spider" deployments during the 2004–2005 eruption of Mount St. Helens, Washington, chap. 16 *of* Sherrod, D.R., Scott, W.E., and Stauffer, P.H., eds., A volcano rekindled; the renewed eruption of Mount St. Helens, 2004–2006: U.S. Geological Survey Professional Paper 1750 (this volume).

Langbein, J., Wyatt, F., Johnson, H., Hamann, D., and Zimmer, P., 1995, Improved stability of a deeply anchored geodetic monument for deformation monitoring: Geophysical Research Letters, v. 22, p. 3533–3536.

Lipman, P.W., Moore, J.G., and Swanson, D.A., 1981, Bulging of the north flank before the May 18 eruption—geodetic data, *in* Lipman, P.W., and Mullineaux, D.R., eds., The 1980 eruptions of Mount St. Helens, Washington: U.S. Geological Survey Professional Paper 1250, p. 143–155.

Magill, J., Wells, R.E., Simpson, R.W., and Cox, A.V., 1982, Post 12 m.y. rotations of southwestern Washington: Journal of Geophysical Research, v. 87, p. 3761–3776.

Mastin, L.G., Roeloffs, E., Beeler, N.M., and Quick, J.E., 2008, Constraints on the size, overpressure, and volatile content of the Mount St. Helens magma system from geodetic and dome-growth measurements during the 2004–2006+ eruption, chap. 22 *of* Sherrod, D.R., Scott, W.E., and Stauffer, P.H., eds., A volcano rekindled; the renewed

eruption of Mount St. Helens, 2004–2006: U.S. Geological Survey Professional Paper 1750 (this volume).

Mazzotti, S., Dragert, H., Henton, J., Schmidt, M., Hyndman, R., James, T., Lu, Y., and Craymer, M., 2003, Current tectonics of northern Cascadia from a decade of GPS measurements: Journal of Geophysical Research, v. 108, no. B12, 2554, doi:10.1029/2003JB002653.

McCaffrey, R., Long, M.D., Goldfinger, C., Zwick, P.C., Nabelek, J.L., Johnson, C.K., and Smith, C., 2000, Rotation and plate locking at the southern Cascadia subduction zone: Geophysical Research Letters, v. 27, no. 19, p. 3117–3120.

McTigue, D.F., 1987, Elastic stress and deformation near a finite spherical magma body; resolution of the point source paradox: Journal of Geophysical Research, v. 92, no. B12, p. 12931–12940.

Menke, W., 1984, Geophysical data analysis; discrete inverse theory: New York, Elsevier, 260 p.

Miller, M.M., Johnson, D.J., Rubin, C.M., Dragert, H., Wang, K., Qamar, A., and Goldfinger, C., 2001, GPS determination of alongstrike variation in Cascadia margin kinematics; implications for relative plate motion, subduction zone coupling, and permanent deformation: Tectonics, v. 20, p. 161–176.

Mogi, K., 1958, Relations between the eruptions of various volcanoes and the deformations of the ground surfaces around them: Bulletin of the Earthquake Research Institute of University of Tokyo, v. 36, p. 99–134.

Murray, M., and Lisowski, M., 2000, Strain accumulation along the Cascadia subduction zone; Cape Mendocino to the Straits of Juan de Fuca: Geophysical Research Letters, v. 27, p. 3631–3634.

Murray, M.H., Marshall, G.A., Lisowski, M., and Stein, R.S., 1996, The 1992 M=7 Cape Mendocino, California, earthquake; coseismic deformation at the south end of the Cascadia megathrust: Journal of Geophysical Research, v. 101, no. B8, p. 17707–17725.

Okada, Y., 1985, Surface deformation due to shear and tensile faults in a half-space: Bulletin of the Seismological Society of America, v. 75, no. 4, p. 1135–1154.

Okada, Y., 1992, Internal deformation due to shear and tensile faults in a half-space: Bulletin of the Seismological Society of America, v. 82, no. 2, p. 1018–1040.

Pallister, J.S., Hoblitt, R.P., Crandell, D.R., and Mullineaux, D.R., 1992, Mount St. Helens a decade after the 1980 eruptions; magmatic models, chemical cycles, and a revised hazards assessment: Bulletin of Volcanology, v. 54, no. 2, p. 126–146, doi: 10.1007/BF00278003.

Preisendorfer, R.W., 1988, Principal component analysis in meteorology and oceanography, *in* Mobley, C.D., ed., Developments in Atmospheric Science 17: New York, Elsevier, 425 p.

Savage, J.C., 1988, Principal component analysis of geodetically measured deformation in Long Valley caldera, eastern California: Journal of Geophysical Research, v. 93, p. 1983–1987.

Savage, J.C., 1995, Principal component analysis of interseismic deformation in southern California: Journal of Geophysical Research, v. 100, p. 12691–12701.

Savage, J.C., and Prescott, W.H., 1973, Precision of Geodolite distance measurements for determining fault movements: Journal of Geophysical Research, v. 78, p. 6001–6008.

Savage, J.C., Prescott, W.H., and Gu, G., 1986, Strain accumulation in southern California, 1973–1984: Journal of Geophysical Research, v. 91, p. 7455–7473.

Savage, J.C., Lisowski, M., and Prescott, W.H., 1991, Strain accumulation in western Washington: Journal of Geophysical Research, v. 96, p. 14493–14507.

Savage, J.C., Lisowski, M., and Prescott, W.H., 1996, Observed discrepancy between Geodolite and GPS distance measurements: Journal of Geophysical Research, v. 101, p. 25547–25552.

Savage, J.C., Svarc, J.L., Prescott, W.H., and Murray, M.H., 2000, Deformation across the forearc of the Cascadia subduction zone at Cape Blanco, Oregon: Journal of Geophysical Research, v. 105, no. B2, p. 3095–3102.

Savage, J.C., Gan, W., and Svarc, J.L., 2001, Strain accumulation and rotation in the Eastern California Shear Zone: Journal of Geophysical Research, v. 106, no. B10, p. 21995–22007.

Schilling, S.P., Thompson, R.A., Messerich, J.A., and Iwatsubo, E.Y., 2008, Use of digital aerophotogrammetry to determine rates of lava dome growth, Mount St. Helens, Washington, 2004–2005, chap. 8 *of* Sherrod, D.R., Scott, W.E., and Stauffer, P.H., eds., A volcano rekindled; the renewed eruption of Mount St. Helens, 2004–2006: U.S. Geological Survey Professional Paper 1750 (this volume).

Simpson, R.W., and Cox, A.V., 1977, Paleomagnetic evidence for tectonic rotation of the Oregon Coast Range: Geology, v. 5, p. 585–598.

Smith, K.D., von Seggern, D., Blewitt, G., Preston, L., Anderson, J.G., Wernicke, B.P., and Davis, J.L., 2004, Evidence for deep magma injection beneath Lake Tahoe, Nevada–California: Science, v. 305, no. 5688, p. 1277–1280.

Svarc, J.L., Savage, J.C., Prescott, W.H., and Murray, M.H., 2002, Strain accumulation and rotation in western Oregon and southwestern Washington: Journal of Geophysical

Research, v. 107, no. B5, 2087, doi:10.1029/2000JB000033.

Swanson, D.A., Lipman, P.W., Moore, J.G., Heliker, C.C., and Yamashita, K.M., 1981, Geodetic monitoring after the May 18 eruption, *in* Lipman, P.W., and Mullineaux, D.R., eds., The 1980 eruptions of Mount St. Helens, Washington: U.S. Geological Survey Professional Paper 1250, p. 157–168.

Verdonck, D., 2006, Contemporary vertical crustal deformation in Cascadia: Tectonophysics, v. 417, nos. 3–4, p. 221–230.

Wdowinski, S., Bock, Y., Zhang, J., Fang, R., and Genrich, J.F., 1997, Southern California Permanent GPS Geodetic Array; spatial filtering of daily positions for estimating coseismic and postseismic displacements induced by the 1992 Landers earthquake: Journal of Geophysical Research, v. 102, no. B8, p. 18057–18070.

Webb, F.H., and Zumberge, J.F., 1995, An introduction to GIPSY/OASIS-II: Pasadena, Calif., Jet Propulsion Laboratory Publication No. JPL D-11088.

Wells, R.E., and Simpson, R.W., 2001, Northward migration of the Cascadia forearc in the northwestern U.S. and implications for the subduction deformation: Earth, Planets and Space, v. 53, p. 275–283.

Wells, R.E., Weaver, C.S., and Blakely, R.J., 1998, Fore-arc migration in Cascadia and its neotectonic significance: Geology, v. 26, no. 8, p. 759–762.

Williams, S.D., Bock, Y., Fang, P., Jamason, P., Nikolaidis, R.M., Prawirodirdjo, L., Miller, M., and Johnson, D.J., 2004, Error analysis of continuous GPS position time series: Journal of Geophysical Research, v. 109, no. B03412, doi:10.1029/2003JB00274.

Yang, X., Davis, P.M., and Dieterich, J.H., 1988, Deformation from inflation of a dipping finite prolate spheroid in an elastic half-space as a model for volcanic stressing: Journal of Geophysical Research, v. 93, no. B5, p. 4289–4257.

Zumberge, J.F., Heflin, M.B., Jefferson, D.C., Watkins, M.M., and Webb, F.H., 1997, Precise point positioning for the efficient and robust analysis of GPS data from large networks: Journal of Geophysical Research, v. 102, no. B3, p. 5005–5017.